

PCCP

Accepted Manuscript



This is an *Accepted Manuscript*, which has been through the Royal Society of Chemistry peer review process and has been accepted for publication.

Accepted Manuscripts are published online shortly after acceptance, before technical editing, formatting and proof reading. Using this free service, authors can make their results available to the community, in citable form, before we publish the edited article. We will replace this *Accepted Manuscript* with the edited and formatted *Advance Article* as soon as it is available.

You can find more information about *Accepted Manuscripts* in the [Information for Authors](#).

Please note that technical editing may introduce minor changes to the text and/or graphics, which may alter content. The journal's standard [Terms & Conditions](#) and the [Ethical guidelines](#) still apply. In no event shall the Royal Society of Chemistry be held responsible for any errors or omissions in this *Accepted Manuscript* or any consequences arising from the use of any information it contains.

Toward the Design of Alkynylimidazole Fluorophores: Computational and Experimental Characterization of Spectroscopic Features in Solution and in Poly(methyl methacrylate)

Vincenzo Barone^a, Fabio Bellina^b, Malgorzata Biczysko^{*c}, Julien Bloino^c, Teresa Fornaro^a, Camille Latouche^a, Marco Lessi^b, Giulia Marianetti^{a,b}, Pierpaolo Minei^{a,b}, Alessandro Panattoni^a, Andrea Pucci^b

Received Xth XXXXXXXXXXXX 20XX, Accepted Xth XXXXXXXXXXXX 20XX

First published on the web Xth XXXXXXXXXXXX 200X

DOI: XXX

The possibilities offered by organic fluorophores in the preparation of advanced plastic materials have been increased by designing novel alkynylimidazole dyes, featuring different push and pull groups. This new family of fluorescent dyes was synthesized by means of a one-pot sequential bromination-alkynylation of the heteroaromatic core, and their optical properties were investigated in tetrahydrofuran and in poly(methyl methacrylate). An efficient *in silico* pre-screening scheme was devised as consisting of a step-by-step procedure employing computational methodologies by simulation of electronic spectra within simple vertical energy and more sophisticated vibronic approaches. Such an approach was also extended to efficiently simulate one-photon absorption and emission spectra of the dyes in the polymer environment for their potential application in luminescent solar concentrators. Besides the specific applications of this novel material, the integration of computational and experimental techniques reported here provides an efficient protocol that can be applied to make a selection among similar dye candidates, which constitute the essential responsive part of those fluorescent plastic materials.

1 Introduction

Nowadays, organic fluorophores with a delocalized π -conjugated system represent fundamental and ripe components of many advanced functional materials. Leading examples are based on active substances in organic electronics¹, photovoltaics²⁻⁴, solar concentration^{5,6} and chromogenic systems^{7,8}. Among others, (hetero)aromatic π -conjugated systems usually display large photoresponses in a spectral region that can be easily tuned from the visible to the near infrared by strategic functional groups embedded in the main chromophoric core. Furthermore, these systems show increased stability and thermal and chemical robustness required for the fabrication of modern advanced materials.

Quite often, however, the choice of the best candidate for the application of interest is hardly achievable through chem-

ical intuition alone, since the effect on the spectral features of the chromophore (i.e. absorption and emission maxima and intensities, Stokes shift and quantum yield) by changing the nature of the functional groups is not easily predictable. Indeed, while experimental absorption and emission spectra contain this information, they are generally the result of a multitude of contributing effects, so relating the band-shape to the properties of the bare molecule may be a difficult task. As a result, a selection process based on those data alone can be very approximate and require a significant number of trial-and-error attempts in order to get the chromophore with the best performance, increasing significantly the synthetic effort, and so the overall cost.

Alternatively, a more systematic study can be achieved with computational modeling, which offers the possibility to get a better understanding of the chemical-physical properties at the origin of the observed spectra. In fact, computational methods give an insight on the structural and stereo-electronic molecular properties, in both the ground and excited electronic states⁹⁻¹⁴ mimicking the real molecular environment for instance by means of Polarizable Continuum Models (PCM)¹⁵⁻²¹ or more complex matrices where the chromophores can be incorporated.²²⁻²⁵ Moreover, state-of-the-art computational techniques have shown excellent performance not only in predicting vertical absorption and emission transi-

† Electronic Supplementary Information (ESI) available: (i) atomic charges from natural bond orbital analysis for the **1b** and **2b** chromophores; (ii) typical responsivity curve of photodiodes. See DOI: 10.1039/b000000x/

^a Scuola Normale Superiore, piazza dei Cavalieri 7, I-56126 Pisa, Italy

^b Dipartimento di Chimica e Chimica Industriale, Università di Pisa, via Moruzzi 13, I-56124 Pisa, Italy

^c Consiglio Nazionale delle Ricerche, Istituto di Chimica dei Composti OrganoMetallici (ICCOM-CNR), UOS di Pisa, Area della Ricerca CNR, Via G. Moruzzi 1, I-56124 Pisa, Italy; e-mail: malgorzata.biczysko@pi.iccom.cnr.it

tions, but also to simulate realistic spectral shapes^{26–28}.

Nowadays it is well recognized that computational strategies based on the density functional theory (DFT) and its time-dependent extension (TD-DFT) allow for rationalisation and effective design of novel chromophores^{12,14}. However, the standard approach is still based on the computation of the ground and excited state properties, frontier molecular orbitals and energies and oscillator strengths of vertical excitations (VE), which are eventually convoluted by phenomenological (mostly symmetrical) distribution functions^{12,29,30}. Only recently the direct simulation of the electronic spectra line-shape with a proper account of vibrational effects^{26,27,31} become feasible for routine studies of larger molecular systems^{14,25,28}. Inclusion of vibronic effects is not only crucial for the interpretation of high-resolution data showing a detailed vibrational structure^{32,33} but also for low-resolution spectra, allowing to simulate realistic asymmetric band-shapes and to account correctly for the relative intensities of transitions^{34,35}, including also vibronic effects on the emission spectra⁸. An efficient *in silico* pre-screening scheme can be devised by combination of standard and more sophisticated computations into a step-by-step procedure. It has been already shown that a combination of cheap approaches based on vertical excitations with more advanced vibronic models to simulate absorption and emission electronic spectra, can provide feasible and accurate computational pre-screening schemes for semi-rigid chromophores⁸. This theoretical analysis can effectively guide the synthetic work favouring a rational molecular design, with clear benefits in terms of cost and time.⁸ In practice, once an interesting molecular candidate has been identified experimentally, a virtual screening³⁶ of the UV/Vis absorption and emission properties can be performed on a wide set of homologues with the same skeletal structure (the actual chromophoric unit) but different electron donor and acceptor groups (called push and pull groups, respectively) in order to select one or more target molecules on which experiments can be focused. In this work we extend such a protocol to more flexible chromophores taking into account also nonspecific effects of amorphous polymer matrices.

Herein, we report on a combined computational and experimental study of the spectroscopic properties for a family of newly synthesized heteroaromatic chromophores by sequential regioselective bromination-alkynylation of the heterocyclic core. More specifically, the work is focused on the phenylethynyl-phenylimidazole backbone functionalised by different push (R_X : OMe) and pull (R_Y : NO₂, COOEt) groups, namely the Y_X derivatives in Scheme 1, aimed at assessing their fluorescent properties and proving the ground for further *in silico* screening studies. Eventually, the optical features of the nitro derivatives are also determined when dispersed in a transparent amorphous polymer matrix such as poly(methyl methacrylate), for their potential application in

luminescent solar concentrators (LSC).

2 Experimental Section

2.1 Materials

Melting points were recorded on a hot-stage microscope (Reichert Thermovar). Fluka precoated 60 F254 aluminium silica gel sheets were used for TLC analyses. GLC analyses were performed using two types of capillary columns: an Alltech AT-35 bonded FSOT column (30 m x 0.25 mm i.d.) and an Alltech AT-1 bonded FSOT column (30 m x 0.25 mm i.d.). Purifications by flash-chromatography were performed using silica gel Merck 60 (particle size 0.040–0.063 mm). EI-MS spectra were measured at 70 eV by GLC/MS. NMR spectra were recorded at room temperature at 200 MHz (¹H) and 50.3 MHz (¹³C) and were referred to TMS or to the residual protons of deuterated solvents. All reactions were performed under argon, by standard syringe, cannula and septa techniques. *N,N*-dimethylformamide (DMF) and *N,N*-dimethylacetamide (DMA) were dried by distillation at reduced pressure over CaH₂. 1-methyl-1*H*-imidazole (**4**) was purified by distillation at reduced pressure. Phenylacetylene (**7a**), 4-ethynylanisole (**7b**), and piperidine were purified by distillation at reduced pressure over CaH₂. *N*-bromosuccinimide (NBS) was purified by crystallization. All the other commercially available reagents and solvents were used as received. Ethyl 4-(1-Methyl-1*H*-imidazol-2-yl)benzoate (**3b**) was prepared by the Pd/Cu-mediated direct C-2 arylation of 1-methyl-1*H*-imidazole (**4**) with ethyl 4-bromobenzoate (**5b**) as previously reported³⁷.

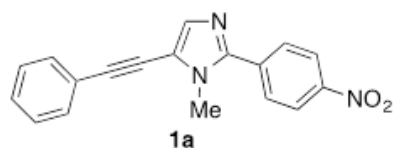
Poly(methyl methacrylate) (PMMA, Aldrich, M_w = 350,000 g/mol, acid number <1 mg KOH/g) density = 1.17 g/mL (T = 15° C).

2.1.1 1-Methyl-2-(4-nitrophenyl)-1*H*-imidazole (3a) A modification of the literature procedure for the Pd- and Cu-mediated C-2 arylation of 1-substituted-1*H*-imidazole with aryl bromides was adopted³⁸. A solution of 1-methyl-1*H*-imidazole (**4**) (5.0 mmol, 0.41 g, 0.40 mL), Pd(OAc)₂ (56 mg, 0.25 mmol), CuI (1.9 g, 10.0 mmol) and 1-bromo-4-nitrobenzene (**5a**) (1.52 g, 7.5 mmol) in DMA (25 mL) was stirred at 160° C for 72h. After being cooled to room temperature the reaction mixture was diluted with AcOEt (100 mL) and poured into a saturated aqueous NH₄Cl solution (100 mL). NH₄OH (5 mL) was added and the resulting mixture was stirred in the open air for 0.5 h and then extracted with AcOEt. The organic extract was washed with water, dried over anhydrous Na₂SO₄, filtered through Celite and the filtrate was concentrated under reduced pressure. The crude reaction product was purified by flash chromatography on silica gel with EtOAc as eluent to give **3a** as a yellow solid (1.02 g, 82%), m.p.: 108–111° C. EIMS, *m/z* (%): 324 (25), 323 (100), 278 (7), 277

(34), 231 (17). ^1H NMR (200 MHz, CDCl_3): δ = 8.30 (m, 2H), 7.87 (m, 2H), 7.18 (d, J = 1.2 Hz, 1H), 7.08 (d, J = 1.2 Hz, 1H), 3.86 (s, 3H) ppm. ^{13}C NMR (50.3 MHz, CDCl_3): δ = 147.2, 145.1, 136.5, 129.3 (2C), 128.8 (2C), 124.0, 123.9, 121.7, 34.9 ppm. Anal. Calcd found: C, 59.16; H, 4.45; N, 20.63. Calc. for $\text{C}_{10}\text{H}_9\text{N}_3\text{O}_2$: C, 59.11; H, 4.46; N, 20.68.

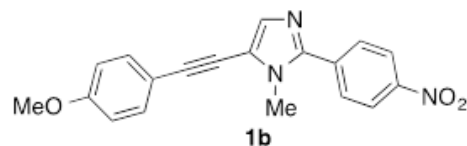
2.2 General procedure for the one-pot C5 halogenation/alkynylation of 2-aryl-1-methyl-1H-imidazoles 3a,b: synthesis of fluorophores 1a,b and 2a,b

To a solution of 2-aryl-1-methyl-1H-imidazole **3** (1 mmol) in DMF (5 mL), NBS (169 mg, 0.95 mmol) was added and the resulting reaction mixture was stirred in the dark at room temperature for 5 h. Then, $\text{Pd}(\text{PPh}_3)_2\text{Cl}_2$ (14 mg, 0.02 mmol, 2 mol%), CuI (8 mg, 0.04 mmol, 4 mol%), an alkyne **7** (1,1 mmol) and piperidine (300 μL , 255 mg, 3 mmol) were added and the resulting reaction mixture was stirred at 80° C for 3 h. The reaction mixture was diluted with EtOAc (100 mL), then saturated aqueous NH_4Cl (100 mL) was added. The resulting mixture was stirred for 30 minutes and extracted with EtOAc (3 x 25 mL). The organic extracts were washed with water (3 x 25 mL) and brine (1 x 25 mL), dried over anhydrous Na_2SO_4 , filtered and concentrated under reduced pressure. The residue was purified by flash chromatography on silica gel. This procedure was employed to prepare compounds **1a,b** and **2a,b**. GLC analysis showed that all these compounds had chemical purity higher than 98%.

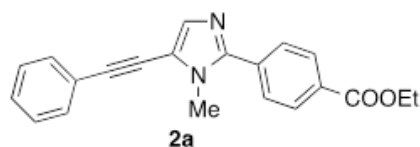


2.2.1 1-Methyl-2-(4-nitrophenyl)-5-(phenylethynyl)-1H-imidazole (1a) The crude reaction product obtained by the one-pot halogenation/alkynylation reaction of 1-methyl-2-(4-nitrophenyl)-1H-imidazole (**3a**) with phenylacetylene (**7a**) was purified by flash chromatography on silica gel with a mixture of toluene and EtOAc (90:10) as eluent to give **1a** as an orange solid (205 mg, 81%), m.p.: 154-157° C. EIMS, m/z (%): 304 (21), 303 (100), 257 (19), 256 (13), 255 (9). ^1H NMR (200 MHz, CDCl_3): δ = 8.34 (m, 2H), 7.90 (m, 2H), 7.55 (m, 2H), 7.49 (s, 1H), 7.39 (m, 3H), 3.89 (s, 3H) ppm. ^{13}C NMR (50.3 MHz, CDCl_3): δ = 147.5, 145.8, 136.1, 134.5, 131.3 (2C), 129.0 (2C), 128.9, 128.5 (2C), 123.9 (2C), 122.1, 119.5, 97.8, 77.1, 33.3 ppm. Anal. Calcd found: C, 71.35; H, 4.33; N, 13.88. Calc. for $\text{C}_{18}\text{H}_{13}\text{N}_3\text{O}_2$: C, 71.28; H, 4.32; N, 13.85.

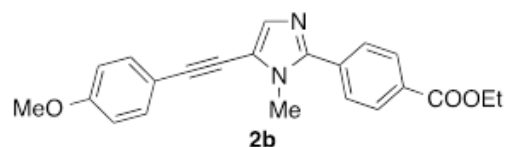
2.2.2 5-((4-Methoxyphenyl)ethynyl)-1-methyl-2-(4-nitrophenyl)-1H-imidazole (1b) The crude reaction product



obtained by one-pot halogenation/alkynylation reaction of 1-methyl-2-(4-nitrophenyl)-1H-imidazole (**3a**) with 4-ethynylanisole (**7b**) was purified by flash chromatography on silica gel with a mixture of toluene and EtOAc (90:10) as eluent to give **1b** as a red solid (144 mg, 72%), m.p.: 168-171° C. EIMS, m/z (%): 334 (22), 333 (100), 318 (13), 303 (10), 287 (10). ^1H NMR (200 MHz, CDCl_3): δ = 8.33 (m, 2H), 7.89 (m, 2H), 7.48 (m, 2H), 7.27 (s, 1H), 6.91 (m, 2H), 3.88 (s, 3H), 3.85 (s, 3H) ppm. ^{13}C NMR (50.3 MHz, CDCl_3): δ = 160.1, 147.5, 145.6, 136.2, 134.1, 132.9 (2C), 128.9 (2C), 123.9 (2C), 119.9, 114.2 (2C), 97.8, 75.8, 55.4, 33.3 ppm. Anal. Calcd found: C, 68.50; H, 4.55; N, 12.59. Calc. for $\text{C}_{19}\text{H}_{15}\text{N}_3\text{O}_3$: C, 68.46; H, 4.54; N, 12.61.



2.2.3 Ethyl 4-(1-methyl-5-(phenylethynyl)-1H-imidazol-2-yl)benzoate (2a) The crude reaction product obtained by one-pot halogenation/alkynylation reaction of ethyl 4-(1-methyl-1H-imidazol-2-yl)benzoate (**3b**) with phenylacetylene (**7a**) was purified by flash chromatography on silica gel with a mixture of toluene and EtOAc (90:10) as eluent to give **2a** as a brown solid (211 mg, 74%), m.p.: 123-126° C. EIMS, m/z (%): 330 (100), 302 (15), 301 (17), 257 (8), 128 (8). ^1H NMR (200 MHz, CDCl_3): δ = 8.15 (m, 2H), 7.77 (m, 2H), 7.52 (m, 2H), 7.47 (s, 1H), 7.36 (m, 2H), 4.40 (q, J = 7.1 Hz, 2H), 3.82 (s, 3H), 1.41 (t, J = 7.1, 3H) ppm. ^{13}C NMR (50.3 MHz, CDCl_3): δ = 165.8, 147.1, 134.1, 134.0, 131.1 (2C), 130.4, 129.6 (2C), 128.5, 128.3 (2C), 128.1 (2C), 122.2, 118.5, 97.1, 77.5, 61.0, 33.0, 14.2 ppm. Anal. Calcd found: C, 76.38; H, 5.50; N, 20.63. Calc. for $\text{C}_{21}\text{H}_{18}\text{N}_2\text{O}_2$: C, 76.34; H, 5.49; N, 20.65.



2.2.4 Ethyl 4-(5-((4-methoxyphenyl)ethynyl)-1-methyl-1H-imidazol-2-yl)benzoate (2b) The crude reaction

product obtained by one-pot halogenation/alkynylation reaction of ethyl 4-(1-methyl-1*H*-imidazol-2-yl)benzoate (**3b**) with 4-ethynylanisole (**7b**) was purified by flash chromatography on silica gel with a mixture of toluene and EtOAc (80:20) as eluent to give **2b** as a yellow solid (158 mg, 90%), m.p.: 141-145 °C. EIMS, *m/z* (%): 361 (25), 360 (100), 345 (7), 332 (11), 317 (14). ¹H NMR (200 MHz, CDCl₃): δ = 8.15 (m, 2H), 7.76 (m, 2H), 7.47 (m, 2H), 7.43 (s, 1H), 6.89 (m, 2H), 4.40 (q, *J* = 7.4 Hz, 2H), 3.83 (s, 3H), 3.82 (s, 3H), 1.41 (t, *J* = 7.4 Hz, 3H) ppm. ¹³C NMR (50.3 MHz, CDCl₃): δ = 165.9, 159.9, 147.0, 134.3, 133.7, 132.8 (2C), 130.4, 129.7 (2C), 128.2 (2C), 118.9, 114.3, 114.1 (2C), 97.1, 76.1, 61.1, 55.3, 33.1, 14.3 ppm. Anal. Calcd found: C, 73.37; H, 5.58; N, 7.79. Calc. for C₂₂H₂₀N₂O₃: C, 73.32; H, 5.59; N, 7.77.

2.3 Preparation of polymer films for optical studies

Different dye/PMMA thin films were prepared by drop casting, i.e. pouring a 0.8 mL chloroform solution containing 30 mg of the polymer and the proper amount of dye to obtain concentrations in the range of 0.05-2.2 wt.% over a 35x50 mm area of a glass surface. The glass slides were cleaned with chloroform and immersed in 6 M HCl for at least 12 h, then they were rinsed with water, acetone and isopropanol and dried for 8 h at 120 °C. Solvent evaporation was performed on a warm hot plate (about 30 °C) and in a closed environment. The film thickness was measured by a Starrett micrometer to be 25±5 μm. The PMMA films were easily removed with a spatula after immersion in water so that they can be stored for successive measurements and comparison by attaching them on 50x50x3 mm optically pure glass substrate (Edmund Optics Ltd BOROFLOAT window 50x50 TS) with a high-purity silicone oil with a refractive index comparable to PMMA and glass (i.e., poly(methylphenyl siloxane), 710 fluid, Aldrich, refractive index *n* = 1.5365). Absorption and emission properties of such devices showed negligible differences with the freshly prepared ones.

Apparatus and Methods

Absorption spectra were recorded at room temperature on a Perkin-Elmer Lambda 650 spectrometer. Fluorescence spectra were measured at room temperature on a Horiba Jobin-Yvon Fluorolog®-3 spectrofluorometer and equipped with a 450 W xenon arc lamp, double-grating excitation and single-grating emission monochromators. The fluorescence of dye/PMMA films were recorded by using the Solid-Sample Holder and collecting the front-face emission at 30°.

The fluorescence quantum yield (Φ_f) in tetrahydrofuran (THF) was determined at room temperature relative to quinine sulphate ($\Phi_f^S = 0.54$ in 0.1 M H₂SO₄) using the following relation:

$$\Phi_x = \Phi_{ST} \left(\frac{\text{Grad}_X}{\text{Grad}_{ST}} \right) \left(\frac{\eta_X^2}{\eta_{ST}^2} \right)$$

Where the subscripts ST and X are standard and dye respectively, “Grad” is the gradient from the plot of integrated fluorescence intensity versus absorbance for different solutions of standard and dyes. In order to minimise re-absorption effects concentration was kept low, so absorbances never exceed 0.1 at and above the excitation wavelength. η is the refractive index of the solvent, i.e. 1.405 for THF and 1.333 for water³⁹. A thin film of about 10⁻³ M 9,10-diphenylanthracene in PMMA was used as a standard ($\Phi_f^S = 0.83$)⁴⁰ for the quantum yield measurement of dye/PMMA films.

Photocurrent measurements

A proper apparatus was built, made of a plywood wooden box 15x15x30 cm with walls 1.5 cm thick. A removable cover hosting a housing for a solar lamp is present at the top. During the measurement a solar lamp TRUE-LIGHT® ESI E27 20W was used. Two 50x3 mm slits were carved out at 5 cm from the bottom of the box to exactly fit the LSC systems (dimensions 50x50x3 mm) so that a minimum amount of light would come out during the measurements. On the outer side of the slit, a set of three 1x1 cm photodiodes (THORLABS FDS1010 Si photodiode, with an active area of 9.7 x 9.7 mm and high responsivity (A/W) in the spectral range of 400-1100 nm) connected in parallel fashion was placed and coupled to a multimeter (KEITHLEY Mod. 2700) for photocurrent measuring.

Efficiency measurement using a PV-cell

A different set of LSC samples was prepared to measure the concentration efficiency attaching a Si-PV cell (IXYS SLMD121H08L mono solar cell 86x14 mm, with a solar cell efficiency of 22% and a fill factor > 70%) to one edge of the sample. This set of samples was made covering the full 50x50 mm area of the previously introduced optically pure glass slabs with a 24±5 μm dye/PMMA thick film. One edge of the LSC was connected to a Si-based PV cell masked to cover just the LSC edge (50x3 mm) using silicone grease while the remaining edges were covered with an aluminum tape. These devices were then placed over a white poly(ethylene terephthalate) scattering sheet (Microcellular® MCPET reflective sheet, ERGA TAPES Srl) and placed about 20 cm under a solar lamp (TRUELIGHT®ESL E27 20W, with a correlated color temperature of 5500 K). The efficiency is reported as η_{opt} , which is the ratio between the short circuit current of the PV cell attached the LSC edges under illumination of a light source (I_{LSC}) and the short circuit current of the bare cell put perpendicular to the light source (I_{SC}).

3 Computational Methods

Quantum mechanical (QM) calculations on fluorophores **1a,b** and **2a,b** have been performed at the density functional theory (DFT) and its time-dependent extension (TD-DFT) levels of theory.⁴¹⁻⁴⁴ Due to the likely presence of long-distance

charge transfers, the CAM-B3LYP functional⁴⁵ has been chosen, together with the SNSD basis set^{46,47}, which was developed for spectroscopic studies of medium-to-large molecular systems. The SNSD basis set allows cost-effective predictions for a broad range of spectroscopic properties, including electronic absorption and emission spectra^{10,27}. Vertical excitation energies (VE) and excited state equilibrium geometries have been calculated with TD-DFT⁴⁸. As a matter of fact, the TD-CAM-B3LYP computations have already shown very good performance for a broad range of excited electronic states^{49,50}, and in conjunction with the SNSD or N07D-aug basis sets they have been extensively tested for spectroscopic properties of different π -conjugated chromophores^{8,25,28}.

In order to match experimental conditions, environmental effects simulating solvent (THF) and polymeric matrix (PMMA) have been accounted for with the polarizable continuum model (PCM)^{17–19,51} and more precisely its Conductor-like (C-PCM) variant²⁰. The molecule-shaped cavity surrounding the solute molecule has been built by interlocking spheres centered on heavy atoms, exploiting the default set of sphere radii implemented in GAUSSIAN⁵². Non-equilibrium solvent effects on the vertical excitation energies have been computed with the linear response LR-PCM/TD-DFT approach^{48,53}, where the excitation energies are directly determined without computing the exact excited electron density. This solvation model provides reliable results at a relatively low computational cost and can be extended to several spectroscopic properties²¹, with further consideration of spectral line shapes.^{8,25,54}

The TD-CAM-B3LYP/PCM(THF) method has been validated and compared to the TD-B3LYP results based on the computation of vertical absorption energies and the simulation of absorption spectra with respect to their experimental counterparts (see the Results section). Details about the nature of the electronic transitions have been revealed by computation of the electronic densities at the ground and excited states, and the subsequent natural bond orbital (NBO) analysis⁵⁵.

In a first approximation, the electronic spectra can be simulated with the commonly used basic vertical energy approach, which relies on the computation of vertical excitation energies, giving rise to a single peak per electronic transition with the intensity determined by the corresponding electronic transition dipole moment. The line-shapes are then obtained by applying a symmetric distribution functions to simulate the broadening observed experimentally. Nevertheless, the computation of electronic spectra with the VE approach completely neglects the influence of nuclear motions. Therefore, this approach is not able to simulate the vibrational structure present in experimental spectra and, consequently, accurately reproduce the typical asymmetry of the experimental bands, which is often required in order to get more accurate absorption and emission maxima and to be able to correctly interpret the experi-

mental results.^{10,28,56} In this regard, several approaches to include vibronic contributions have recently become feasible for medium-to-large systems, following the time-independent⁵⁶ or time-dependent^{31,57} frameworks. Here we employ the time-independent Franck-Condon Vertical-Gradient (FC|VG) and Adiabatic-Shift (FC|AS) models, which allow to avoid the expensive computations of excited state frequencies. Within the framework of the Franck-Condon principle,^{58–60} the transition dipole moment is assumed to remain constant during the electronic transition, equal to its value at the equilibrium geometry. This approximation is generally valid for fully allowed transitions, such as the ones considered in this work. The spectrum is simulated based on the computation of overlap integrals (Franck-Condon integrals) between the vibrational wavefunctions of the electronic states involved in the transition, which within sum-over-states approach are treated individually (see Refs.^{26,27} for further details). Finally the resulting stick spectrum is convoluted by mean of distribution functions.

In order to compute vibrationally resolved electronic spectra different models are now available, which differ by their conceptual approach to the electronic transition, vertical or adiabatic^{25,56,61}. In this work we will simulate absorption spectra by means of the vertical gradient model, which focuses on the final-state PES at the equilibrium geometry of the initial state, i.e., the region corresponding to the most intense transitions (FC|VG). This is also known in literature as the linear coupling model (LCM)⁶². The adiabatic approach has been applied as well in order to estimate Franck-Condon factors of the emission spectra and simulate fluorescence spectra in polymer matrix, within the Adiabatic Shift (AS) model. Those models (VG and AS) have been applied assuming that the computation of the excited-state energy gradients (at the ground-state equilibrium structure) or excited-state geometry optimizations, are sufficient to describe the PES of excited states in vertical region (absorption, VG) or at its equilibrium (emission, AS) (see Refs.^{27,56,61} for detailed discussions).

The simulated VG and AS stick spectra have been convoluted using Gaussian functions with half-widths at half-maximum (HWHM) of 750 cm^{-1} . This value has been chosen to match the reference experimental absorption spectra.

All computations were performed using a locally modified version of the GAUSSIAN package⁵². A graphical user interface (VMS-Draw)⁶³ was used to analyze in detail the outcome of vibronic computations and plot electronic spectra.

4 Results and Discussion

4.1 Synthesis and experimental characterization of chromophores

5-Alkynyl-2-arylimidazoles **1a,b** and **2a,b** were obtained according to a simple and scalable synthetic procedure involving as the key step a one-pot sequential regioselective C5 bromination and Sonogashira coupling recently described by us (Scheme 2)³⁷. In detail, 2-arylimidazoles **3a,b** were efficiently prepared by a palladium and copper mediated base-free and ligandless direct C2-H arylation reaction, involving 1-methyl-1*H*-imidazole (**4**) and bromoarenes **5a,b**. The 2-arylimidazoles **3a,b** obtained this way were then regioselectively brominated at C5 by reaction with NBS in DMF at room temperature, and to the resulting 2-aryl-5-bromoimidazoles **6a,b** PdCl₂(PPh₃)₂ (2 mol%), CuI (4 mol%), and an arylalkyne **7a,b** (1.1 equiv) were sequentially added. The reaction mixture was then warmed up to 80 °C and stirred for 3 h at this temperature. In this way the fluorophores **1a,b** and **2a,b** were isolated in 72-90% yield (Scheme 2).

Compounds **2a** and **2b** appear as dark brown powders, which emits blue-green light. On the contrary, compounds **1a** and **1b** look like reddish solids, which emit yellow and red light, respectively (Figure 1). The optical features of the prepared fluorophores dissolved in THF solutions are reported in Figure 2 and summarized in Table 1. All fluorophores display absorption bands comprised in the interval between 330 and 370 nm, closely associated to the near UV range of the electromagnetic spectrum of light. In the range of concentration investigated (10⁻⁶-5·10⁻⁵ M), no absorption bands attributed to dyes aggregates emerged. As expected the **1a** and **1b** compounds showed absorption at longer wavelengths than **2a** and **2b** due to the stronger electron-withdrawing character of the nitro group. This behaviour was also reflected and amplified in emission spectra; **1a** and **1b** emit in the interval between 500 and 600 nm with Stokes shift (S) 70 nm larger than the **2a** and **2b** fluorophores. Notably, the presence of the electron-donating -OMe groups shifts the emission maximum of all fluorophores by about 10-15 nm to longer wavelengths. A worthwhile parameter for making useful comparisons between different fluorophores is the product of the extinction coefficient (ϵ) and the quantum yield (QY). This term is directly proportional to the brightness (B) of the dye, accounting for both the amount of light absorbed and the quantum efficiency of the fluorophore. It is evident that the presence of the nitro group strongly affects both ϵ and QY (Table 1), thus providing poor B values (less than 2×10³ M⁻¹cm⁻¹). The nitro group is actually believed to be a general quencher of fluorescence due to donor-excited photoinduced electron transfer (d-PeT) originating from the excited fluorophore moiety showing strong electron-withdrawing effect⁶⁴. Conversely, the emission prop-

erties of the **2a** and **2b** derivatives are comparable to those of the common bright fluorophores (B over 10⁴ M⁻¹cm⁻¹), such as fluorescein⁶⁵, even if characterized by smaller S than nitro **1** derivatives.

4.2 Theoretical characterization of chromophores

4.2.1 Validation: DFT functional In order to rationalize the spectroscopic properties of the studied chromophores we firstly set up an appropriate computational strategy, in particular we focus on the choice of the method to be applied to compute molecular structures, properties, and spectra. In addition to the **1**- and **2**-derivatives we will also consider two model systems: **1b'**, an analogue of **1b** with OMe replaced by OH ($R_X=OH$, $R_Y=NO_2$) and **2b'**, an analogue of **2b** with OMe and COOEt replaced by OH and COOH, respectively ($R_X=OH$, $R_Y=COOH$), all depicted in Scheme 1. It has been already shown⁸ that lateral methoxy groups can be effectively substituted in computational studies by OH groups, to avoid the problem of methyl rotation with the electronic transition, while in experiment, the methoxy group is preferred over OH, due to the undesired reactivity of the latter.

Geometry optimizations and TD-DFT VE calculations have been performed at B3LYP/SNSD, B3LYP/SNSD/PCM(THF) and CAM-B3LYP/SNSD/PCM(THF) levels of theory, in order to assess the most adequate computational approach to be used in the following studies. The vertical excitation energies of the first bright electronic transition computed with the above mentioned methods at the fully optimized ground-state geometries are listed in Table 2. Comparison with experimental absorption maxima from Table 1 shows that the vertical excitation energies are strongly underestimated using the B3LYP and B3LYP/PCM(THF) methods, while a much better agreement is obtained with CAM-B3LYP/PCM(THF). Moreover, B3LYP computations do not show systematic errors with the blue-shifts of B3LYP/PCM(THF) VE varying from 56 nm for **1b** to 157 nm for **2b**, suggesting also different amount of charge-transfer (CT) character for different compounds (*vide infra*). The B3LYP gas phase results are also closer to experiment than the ones including solvent effects, while for CAM-B3LYP/PCM(THF), the VE results agree with experimental λ_{max} within 20 nm for all compounds. The TD-CAM-B3LYP/SNSD computations in conjunction with the C-PCM model show also that VE of **1b'** and **2b'** match well their methoxy counterparts (**1b** and **2b**), validating the use of these model systems in further studies.

4.2.2 Geometric structure in the ground and first excited electronic state in solution Considering the equilibrium structures in the ground electronic state, as optimized in THF solution, contrary to what suggests the skeletal formula (Figure 1), the planar configurations (C_s symmetry) are first-order

saddle points (one imaginary frequency), while the minima show a slight distortion of the molecule around the phenyl- R_Y moiety (Figure 3). Indeed, the planar configuration is a transition state (TS) between the two equivalent distorted ground state geometries. The energy difference between the planar and distorted configurations is of about 4-5.5 kJ mol⁻¹. For example, the energy differences between the planar (imaginary frequency of about $i40$ cm⁻¹) and the distorted (minimum) configuration in the ground state are 4.3 kJ mol⁻¹ for **1b'** and 5.2 kJ mol⁻¹ for **2b'**, with a 36° and 38° distortion of the dihedral angle between the imidazole and the phenyl-pull moiety, respectively.

The situation is quite different in the first excited state (S_1), where for all chromophores unconstrained geometry optimizations in THF have led to nearly planar configurations (the dihedral angles between the imidazole and the phenyl-pull moiety in the ground state and in the excited state are reported in Table 4). This behavior may be explained based on the features of the molecular orbitals. In particular, during the HOMO-LUMO transition a charge transfer from the phenylethynyl-imidazole moiety to the phenyl- R_X one occurs, causing the planarization of the molecules (*vide infra*). For the model systems **1b'** and **2b'**, the energy difference between the planar configuration (constrained geometry optimisation) and the distorted one have been calculated also in the excited state. As expected, only a slight energy difference in the excited state has been observed, namely 0.1 kJ mol⁻¹ for **1b'** and 0.2 kJ mol⁻¹ for **2b'** with a 10° and 8° distortion of the dihedral angle between the imidazole and the phenyl-pull moiety, respectively. These results indicate that the PES of the excited state is rather flat, while the PES of the ground state is narrower, corresponding to a more rigid structure as shown in Figure 4.

4.2.3 Vertical absorption and emission spectra and molecular orbitals analysis A detailed analysis of molecular orbitals shows that the gap between the HOMO and the LUMO is lower for chromophores with $R_Y=NO_2$ than with $R_Y=COOEt$. This behavior is explained by the stabilization of the LUMO when the nitro moiety is the pull group (Figure 5). Furthermore, when R_X is a push group (OMe, OH), the HOMO is destabilized, resulting in a decrease of the HOMO-LUMO gap. To test the impact of using OH instead of OMe in position R_X , both substitutions have been considered in conjunction with $R_Y=NO_2$ (**1b** and **1b'**). As shown in the molecular orbital diagrams (Figure 5), the HOMO is mainly localized on the phenylethynyl-imidazole moiety for all molecules, while the LUMO is mostly localized on the phenyl-pull moiety. However, with $R_Y=COOEt$, the LUMO is more delocalized than in the case of NO_2 . This can be related to the antibonding character of the delocalized LUMO, which

explains why this orbital is more destabilized than for $R_Y=NO_2$. Moreover, the first bright electronic transition, can be mainly described as HOMO-LUMO, which suggests a charge transfer from the phenylethynyl-imidazole moiety to the phenyl- R_Y ($R_Y=NO_2$, COOEt) one, clearly visible from the plot of the electron density difference (ELD) between the ground and the first excited electronic states shown in Figure 6. Such a plot points out a significant redistribution of the charge during the electron transition, especially in the case of the chromophore with the NO_2 pull group (**1a**). The strong electron-withdrawing effect of the nitro group can be quantified by the analysis of atomic NBO charges presented in Figure 7, showing a significantly larger increase of electron density upon the electronic excitation on the NO_2 ($\Delta=-0.08$) in comparison to the COOEt ($\Delta=-0.02$).

The TD-DFT vertical absorption and emission electronic transitions, computed within the non-equilibrium solvent regime are reported in Table 3. In order to study emission properties, the excited-state geometry (S_1) of each system has been optimized at the TD-DFT level. Concerning the absorption spectra a good agreement between TD-CAM-B3LYP/SNSD/C-PCM(THF) computed excitations and the reference experimental data has been already pointed out. The situation is more challenging for the comparison between the computed and observed fluorescence wavelengths. For compounds **2a** and **2b**, i.e. when the pull moiety is $R_Y=COOEt$, the observed and computed values are very close (discrepancies lower than 15 nm). On the other hand, for **1a** and **1b**, i.e. with NO_2 as the pull moiety, there is a systematic underestimation of about 70 nm. This behavior cannot be ascribed to structural effects since the geometry distortion from the ground state to the excited state seems to be independent of the pull group as shown in Table 4. This larger discrepancy seems to be a purely electronic effect related to intrinsic limits of the TD-DFT model. However, we note that the TD-DFT computations lead to a correct trend as far as the relative positions of absorption and emission maxima, and also the Stokes shifts are concerned: **1b** ≥ **1a** > **2b** ≥ **2a**.

4.2.4 Electronic spectra line-shapes in solution The VE theoretical absorption spectra, convoluted using Gaussian functions with a half-width at half-maximum of 2500 cm⁻¹ are shown in Figure 8 for all chromophores. Although those TD-DFT calculations clearly show two bands in the 250-500 nm range for **1a** and **1b**, our study has been focused on the lower-energy ones for all chromophores. The latter, indeed match rather well the band positions and shapes of the experimental spectra with an average error between calculated and experimental values of the absorption maxima of about 15 nm. Moreover, as already discussed based on the data from Table 3, the experimental trend moving from one chromophore

to the other is computationally well reproduced. In fact, it can be noted that the strong sensitivity of the absorption maximum wavelength on the nature of the push/pull substituents is correctly simulated, showing diagnostic shifts towards different spectral regions depending on the specific push/pull groups.

A significant improvement to the computed electronic spectra can be achieved by taking into proper account the vibrational effects, with the so-called vibronic calculations, which will be considered within the Vertical Gradient approach. The FC|VG model is computationally inexpensive and well suited to the study of low-resolution absorption spectra of strongly allowed transitions. It can be also noted that the changes in the electron density between the ground state and the first excited electronic state obtained at the equilibrium geometry of the ground state (S_0) and the excited state (S_1) (shown in Figures 6 and 11) are very similar, validating the use of the VG approach. The absorption FC|VG spectra shown in Figure 8 point out the increased agreement with experiments. In particular, FC|VG maximum absorption wavelengths agree within about 6 nm with experiment (improvement of about 10 nm with respect to VE) and describe much better the experimental line-shapes. In fact, contrary to the VE spectra, the asymmetry of the band-shape is now clearly visible.

For the chromophores under study it is noteworthy that, contrary to the ground state, the excited-state equilibrium geometry is nearly-planar, which implies a marked distortion associated to the electronic transition. As a consequence, the case of emission is more challenging since the initial state is the excited one, and the considered time-scales involve relaxation to its nearly-planar equilibrium geometry. The adiabatic shift model take into account directly PESs of the initial and final states computed about their respective minima, at the same time avoiding expensive excited state frequency computations. Nevertheless, the large changes in the equilibrium geometries upon excitation from S_0 to S_1 (as shown in Figure 9 for the specific case of **1a**) results, of course, in a strongly reduced overlap integrals between the corresponding vibrational ground states. This leads to a rather low intensity of the simulated emission spectra for all chromophores, as shown in Figure 10 for the model systems **1b'** and **2b'**. However, for the **1a** and **1b** chromophores, showing the most promising properties due to the largest Stokes shift, intensity is further decreased most likely due to the some non-radiative processes i.e. quenching effects via a donor-excited photoinduced electron transfer⁶⁴. Indeed the LUMOs of compounds **1a** and **1b** are less unstable than those of compounds **2a** and **2b**, and this is accompanied by a much larger electron transfer toward the nitro group. Moreover, analysis of the first three excited electronic states shows for **1b'** a low-lying dark state, which might facilitate a non-radiative energy loss and fluorescence quenching, on the contrary, the first two electronic transitions of compound **2b'** are bright (see Table 5).

4.3 Fluorescence properties in polymethyl methacrylate (PMMA): toward luminescent solar concentrators

Owing to the aforementioned properties of **1a** and **1b**, that is S larger than 150 nm and emission shifted to the yellow-red portion of the electromagnetic spectrum of light, these fluorophores were chosen for investigation when dispersed in a transparent and totally amorphous polymer matrix such as PMMA. Aim of this approach was the determination of the optical properties of the derived thin films in terms of their potential use as luminescent solar concentrators. LSCs represent nowadays a promising technology for sunlight harvesting and solar energy conversion and several solutions are engineered for the development of future photovoltaic (PV) technology⁶⁶. LSCs are thin, flat or bulk plates of highly fluorescent materials that absorb sunlight and concentrate most of the resulting fluorescence to their edges by internal reflection⁶⁷. The photoactive elements are organic dyes or luminescent nanoparticles, dispersed in a transparent polymer matrix. The solar radiation is thus conveniently transmitted to PV cells at their edges, even with a cloudy sky. It is worth noting that PV cell efficiencies can be further increased by matching the dye emission with the cell responsivity. This is an efficient approach to solar PV since the intrinsic red-shifting that accompanies fluorescent emission, in **1a** and **1b**, allows to combine the maximum solar emission intensity (at about 500 nm) and the highest PV cell responsivity, i.e. between 500 and 1000 nm.

The optical features of the prepared fluorophores dispersed in PMMA are reported in Figure 13 and summarized in Table 6. **1a** and **1b** fluorophores in PMMA displayed absorption and emission features in accordance to their respective behaviour in THF solution, thus suggesting that the polymer matrix well interact with the guest molecules preventing their aggregation. Also, the calculated QY (0.1) in the polymer was the same of that evaluated in THF. The fact that QY does not decrease in the PMMA can be attributed to the enhanced rigidity of the fluorophore dispersed in the polymer matrix which allows to recover the loss of efficiency often observed upon dispersion. Notably, both films still show very large S values (i.e., ~ 150 nm) and emissions comprised between 450 and 650 nm (Figure 13a), thus making them suitable for LSC applications. In order to assess the performances as LSC, an optically pure 50x50x3 mm glass was coated with PMMA films with a thickness of 25 ± 5 μm .

In Figure 13b, an example of LSC obtained by coating a thin layer of **1b**/PMMA is reported. It is worth noting the amount of light emitted by the dispersed fluorophore and concentrated to the LSC edge. Photocurrent measurements were accomplished with a home-built apparatus (see experimental part) by using a set of three 1x1 cm photodiodes assembled in parallel fashion. Photodiodes are ideal for measuring light sources in LSC emission range by converting the optical power to an

electrical current, allowing for a fast, precise and reproducible response even with different sets of samples. The maximum photocurrents measured with our setup were $44.5 \pm 0.1 \mu\text{A}$ for 1 wt.% **1b**/PMMA and $37.0 \pm 0.1 \mu\text{A}$ for 1 wt.% **1a**/PMMA systems. The higher photocurrent generated by **1b**/PMMA is ascribed to its more red-shifted emission maximum (around 20 nm) than **1a**/PMMA and agrees well with the typical responsivity curve of photodiodes (Figure S1). No significant variation of the photocurrent values were detected by increasing fluorophores concentration in PMMA up to 2 wt.%.

The LSC with the highest photocurrent, i.e. the **1b**/PMMA system, was analyzed by using a Si-based PV cell attached to one edge of the concentrator, as described in the experimental section. The optical efficiency η_{opt} was evaluated from the concentration factor C , which is the ratio between the short circuit current measured in the case of the cell over the LSC edge (I_{LSC}) and short circuit current of the bare cell put perpendicular to the light source (I_{SC}) (eq.1):

$$\eta_{opt} = \frac{I_{LSC}}{I_{SC} \cdot G} \quad (1)$$

where G is the geometrical factor, which is the ratio between the area exposed to the light source and the collecting area. The calculated η_{opt} for the **1b**/PMMA system was lower than 5% and it agrees well with the optical efficiencies of LSC made of PMMA and containing fluorophores with similar characteristics in terms of emission maxima and QY values⁶⁸. Future approaches for η_{opt} enhancement should adopt new synthetic strategies aimed at increasing the fluorophore QY while maintaining S higher than 150.

Computational studies suggested that the quantum yields of potentially promising chromophores **1a** and **1b** in solution are affected by the large geometry changes between the ground and excited electronic structures and the corresponding low FC overlaps. Such geometrical distortions involving rather large functional groups are less likely in the rigid polymeric matrix²⁴. Following such assumption we have set up a simplified computational model in order to simulate spectra in polymers. In particular, during the excited state optimisation the dihedral angle between the imidazole and the phenyl-pull moieties has been fixed to its ground-state value, while all other nuclear degrees of freedom have been relaxed. The resulting S_1 equilibrium structure presented in Figure 9b shows indeed a large overlap with the corresponding ground state structure. Moreover, the electrostatic effects of the polymer have been accounted for by mean of PCM with the dielectric constant corresponding to PMMA ($\epsilon \approx 3.3$). In such case the calculated fluorescence spectra are significantly more intense with respect to their counterparts in THF solution, where full geometry relaxation of the chromophores is allowed. That intensity increase allows to counter-balance the intrinsic quenching effects of the polymer matrix, which otherwise would fur-

ther reduce the observed QY. Both FC|AS emission spectra of **1b'** are presented in Figure 10 showing also that the observed solution-to-polymer blue-shift is reproduced in our simulations, at least qualitatively. Finally the **1a** and **1b'** emission spectra in PMMA are reported in Figure 12. A more detailed analysis of **1a** and **1b** excited-state properties in THF and PMMA (see for instance the similar ELD plots shown for **1a** in Figure 11) confirms that the expected favourable fluorescence properties in polymeric matrix should be attributed to geometrical/steric rather than to electronic effects on the $S_1 \rightarrow S_0$ transition. It can be also postulated that steric hindrance reduces the efficiency of quenching effects, i.e. the second excited state of **1b'** in PMMA shows a non-negligible oscillator strength (see Table 5). Following the current theoretical analysis we propose that an effective *in silico* pre-screening can be performed assuming directly increased rigidity of chromophores in the polymeric matrix, instead of modelling the isolated flexible chromophores in the solution. However, we note that the scheme is still under development and further improvements are necessary including proper account of non-radiative processes affecting emission quantum yields as well as more reliable modeling of polymer matrices²²⁻²⁵.

5 Conclusions

The selection of the best chromophore candidate for a specific application is quite challenging, and an effective combination of experimental design and computational screening may allow to identify the chromophore with the most appropriate absorption/emission features.⁸ In order to perform a virtual screening, a reliable protocol must be preliminarily devised and validated, choosing the best combination of QM model and environment description which allow to compute accurately the geometries, frequencies and vertical excitation energies, which in turn allow the simulation of electronic spectra within simple vertical energy or more sophisticated vibronic approaches. This contribution focused on the evaluation of stereo-electronic and spectroscopic properties of a new family of chromophores characterized by a alkynylimidazole backbone and different push and pull groups. The fluorophores were obtained in good yields (72-90%) and showed optical features in THF, in the visible region, mostly influenced by the nature the electron-withdrawing group.

Firstly, our results indicate that the CAM-B3LYP/PCM(THF) method is the most appropriate to compute vertical excitation energies and simulate absorption spectra, taking into proper account solvation, which represents an important environmental effect strongly affecting the spectral features. Then, the basic VE approach has been used to simulate electronic spectra, providing good predictions for vertical excitation energies and correctly reproducing the strong sensitivity of the absorption maximum wavelength to

the nature of the push/pull substituents. However, a significant improvement has been achieved by computation of the vibrationally-resolved electronic spectra by means of the VG approach, which can be confidently applied to simulate the broad absorption spectral features observed experimentally. With respect to the emission spectra, simulated through adiabatic AS model, it has been found that large changes between equilibrium structures of ground and excited electronic states in solution lead to low fluorescence intensities, with further fluorescence quenching observed for nitro derivatives.

However, considering that our final target is the chromophore dissolved in the polymeric matrix, we have proposed a cost-effective computational protocol to simulate one-photon absorption and emission spectra in the polymer environment. Notably, alkynylimidazole fluorophores with Stokes shift larger than 150 nm and emission shifted to the yellow-red portion of the electromagnetic spectrum of light were selected and dispersed in PMMA. It has been shown that the largest geometry change, unlikely in PMMA, is related to the variation of the dihedral angle between the imidazole and the phenyl-pull moieties. In such case in order to model polymer environment it is sufficient to take into account geometrical constraints by fixing the dihedral angle to its ground state value (along with some bulk electrostatic effects accounted by PCM). Although the steric hindrance has been also postulated to reduce the efficiency of quenching effects, non-radiative processes in the studied chromophores (either intramolecular or associated with the polymer matrix) are not yet fully understood. Experimental results were also discussed in terms of LSC characteristics which were found to agree well with those of LSC made of PMMA and containing fluorophores with similar features in terms of emission maxima and QY values.

Overall, the proposed strategy can be further applied to perform first steps of virtual screening in order to identify the most efficient chromophores to be used in plastic devices such as LSC. It can be suggested, that similar strategy can be also applied for other sets of homologues, once the main unconstrained geometric effects taking place upon electronic excitation are identified. In more general terms, this work further confirms that understanding and simulation of fluorescent properties of chromophores dispersed in semi-rigid environments require proper account for sterical hindrance, with models ranging from effective mean-field approaches to fully atomistic simulations^{22–25} possibly employing non-periodic boundary conditions.

Acknowledgements

The research leading to these results has received funding from the European Union's Seventh Framework Programme (FP7/2007-2013) under grant agreement No. ERC-2012-AdG-320951-DREAMS. This work was supported by the Ital-

ian MIUR from FIRB Futuro in Ricerca project entitled "Progettazione di materiali nanoeterogenei per la conversione di energia solare" (contract no. RBFR122HFZ) and by the Università di Pisa under PRA 2015 (project No. 2015_0038). The DREAMS center (<http://dreams.sns.it>) is acknowledged, for providing the high performance computer facilities used for most of the calculations presented in this work.

References

- 1 S. Allard, M. Forster, B. Souharce, H. Thiem and U. Scherf, *Angew. Chem. Int. Ed.*, 2008, **47**, 4070–4098.
- 2 H. Imahori, T. Uemeyama and S. Ito, *Acc. Chem. Research*, 2009, **42**, 1809–1818.
- 3 Y. Lin, Y. Li and X. Zhan, *Chem. Soc. Rev.*, 2012, **41**, 4245–4272.
- 4 F. Labat, T. Le Bahers, I. Ciofini and C. Adamo, *Acc. Chem. Research*, 2012, **45**, 1268–1277.
- 5 L. Beverina and A. Sanguineti, in *Organic Fluorophores for Luminescent Solar Concentrators*, ed. A. Tiwari, R. Boukherroub and M. Sharon, John Wiley & Sons, Inc., 2014, pp. 317–355.
- 6 W. G. van Sark, *Renewable Energy*, 2013, **49**, 207–210.
- 7 F. Ciardelli, G. Ruggeri and A. Pucci, *Chem. Soc. Rev.*, 2013, **42**, 857–870.
- 8 G. Prampolini, F. Bellina, M. Biczysko, C. Cappelli, L. Carta, M. Lessi, A. Pucci, G. Ruggeri and V. Barone, *Chem. Eur. J.*, 2013, **19**, 1996–2004.
- 9 *Computational Strategies for Spectroscopy, from Small Molecules to Nano Systems.*, ed. V. Barone, John Wiley & Sons, Inc. Hoboken, New Jersey, 2011.
- 10 V. Barone, A. Baiardi, M. Biczysko, J. Bloino, C. Cappelli and F. Lipparini, *Phys. Chem. Chem. Phys.*, 2012, **14**, 12404–12422.
- 11 A. Dreuw and M. Head-Gordon, *Chem. Rev.*, 2005, **105**, 4009–4037.
- 12 D. Jacquemin, E. A. Perpète, I. Ciofini and C. Adamo, *Acc. Chem. Research*, 2009, **42**, 326–334.
- 13 J. Neugebauer, *Phys. Rep.*, 2010, **489**, 1–87.
- 14 A. D. Laurent, C. Adamo and D. Jacquemin, *Phys. Chem. Chem. Phys.*, 2014, **16**, 14334–14356.
- 15 B. Mennucci and R. Cammi, *Continuum Solvation Models in Chemical Physics: Theory and Applications*, Wiley, Chichester, UK, 2007.
- 16 J.-L. Rivail, D. Rinaldi and V. Dillet, *Mol. Phys.*, 1996, **89**, 1521.
- 17 J. Tomasi, B. Mennucci and R. Cammi, *Chem. Rev.*, 2005, **105**, 2999.
- 18 J. Tomasi, *WIREs Comput. Mol. Sci.*, 2011, **1**, 855–867.

- 19 B. Mennucci, *WIREs Comput. Mol. Sci.*, 2012, **2**, 386–404.
- 20 M. Cossi, G. Scalmani, N. Rega and V. Barone, *J. Comput. Chem.*, 2003, **24**, 669.
- 21 A. V. Marenich, C. J. Cramer, D. G. Truhlar, C. A. Guido, B. Mennucci, G. Scalmani and M. J. Frisch, *Chem. Sci.*, 2011, **2**, 2143–2161.
- 22 A. Pedone, G. Prampolini, S. Monti and V. Barone, *Chem. Mater.*, 2011, **23**, 5016–5023.
- 23 A. Pedone, J. Bloino and V. Barone, *J. Phys. Chem. C*, 2012, **116**, 17807–17818.
- 24 N. De Mitri, G. Prampolini, S. Monti and V. Barone, *Phys. Chem. Chem. Phys.*, 2014, **16**, 16573–16587.
- 25 V. Barone, M. Biczysko, J. Bloino, L. Carta and A. Pedone, *Comput. Theoret. Chem.*, 2014, **1037**, 35–48.
- 26 V. Barone, J. Bloino, M. Biczysko and F. Santoro, *J. Chem. Theory Comput.*, 2009, **5**, 540–554.
- 27 J. Bloino, M. Biczysko, F. Santoro and V. Barone, *J. Chem. Theory Comput.*, 2010, **6**, 1256–1274.
- 28 V. Barone, M. Biczysko, M. Borkowska-Panek and J. Bloino, *ChemPhysChem*, 2014, **15**, 3355–3364.
- 29 X. Zhang, L. Chi, S. Ji, Y. Wu, P. Song, K. Han, H. Guo, T. D. James and J. Zhao, *J. Am. Chem. Soc.*, 2009, **131**, 17452–17463.
- 30 S. Ji, J. Yang, Q. Yang, S. Liu, M. Chen and J. Zhao, *J. Org. Chem.*, 2009, **74**, 4855–4865.
- 31 A. Baiardi, J. Bloino and V. Barone, *J. Chem. Theory Comput.*, 2013, **9**, 4097–4115.
- 32 J. Bloino, M. Biczysko, O. Crescenzi and V. Barone, *J. Chem. Phys.*, 2008, **128**, 244105.
- 33 M. H. Palmer, T. Ridley, S. V. Hoffmann, N. C. Jones, M. Coreno, M. de Simone, C. Grazioli, M. Biczysko and A. Baiardi, *J. Chem. Phys.*, 2015, **142**, 134301.
- 34 J. Neugebauer, E. J. Baerends, M. Nooijen and J. Autschbach, *J. Chem. Phys.*, 2005, **122**, 234305.
- 35 L. Carta, M. Biczysko, J. Bloino, D. Licari and V. Barone, *Phys. Chem. Chem. Phys.*, 2014, 2897–2911.
- 36 S. F. Sousa, N. M. F. S. A. Cerqueira, P. A. Fernandes and M. J. Ramos, *Combinatorial Chemistry & High Throughput Screening*, 2010, **13**, 442–453.
- 37 F. Bellina, M. Lessi, G. Marianetti and A. Panattoni, *Tetrahedron Lett.*, 2015, **56**, 3855–3857.
- 38 F. Bellina, C. Calandri, S. Cauteruccio and R. Rossi, *Tetrahedron*, 2007, **63**, 1970–1980.
- 39 G. A. Crosby and J. N. Demas, *J. Phys. Chem.*, 1971, **75**, 991–1024.
- 40 G. G. Guilbault, in *General Aspects of Luminescence Spectroscopy*, ed. G. G. Guilbault, Marcel Dekker, Inc.: New York, 1990, pp. 1–41.
- 41 P. Hohenberg and W. Kohn, *Physical Review*, 1964, **136**, B864.
- 42 W. Kohn and L. J. Sham, *Physical Review*, 1965, **140**, A1133.
- 43 K. Burke, J. Werschnik and E. K. U. Gross, *J. Chem. Phys.*, 2005, **123**, 062206.
- 44 M. E. Casida, *J. Mol. Struct. Theochem*, 2009, **914**, 3–18.
- 45 T. Yanai, D. P. Tew and N. C. Handy, *Chem. Phys. Lett.*, 2004, **393**, 51–57.
- 46 *Double and triple- ζ basis sets of SNS family, are available in the Download section*, <http://dreams.sns.it>, (last visited: 1 February 2015).
- 47 V. Barone, M. Biczysko and J. Bloino, *Phys. Chem. Chem. Phys.*, 2014, **16**, 1759–1787.
- 48 G. Scalmani, M. J. Frisch, B. Mennucci, J. Tomasi, R. Cammi and V. Barone, *J. Chem. Phys.*, 2006, **124**, 094107.
- 49 M. J. G. Peach, T. Helgaker, P. Salek, T. W. Keal, O. B. Lutnaes, D. J. Tozer and N. C. Handy, *Phys. Chem. Chem. Phys.*, 2006, **8**, 558–562.
- 50 M. Isegawa, R. Peverati and D. G. Truhlar, *J. Chem. Phys.*, 2012, **137**, 244104.
- 51 C. J. Cramer and D. G. Truhlar, *Chem. Rev.*, 1999, **99**, 2161–2200.
- 52 M. J. Frisch, G. W. Trucks, H. B. Schlegel, G. E. Scuseria, M. A. Robb, J. R. Cheeseman, G. Scalmani, V. Barone, B. Mennucci, G. A. Petersson, H. Nakatsuji, M. Caricato, X. Li, H. R. Hratchian, A. F. Izmaylov, J. Bloino, G. Zheng, J. L. Sonnenberg, M. Hada, M. Ehara, K. Toyota, R. Fukuda, J. Hasegawa, M. Ishida, T. Nakajima, Y. Honda, O. Kitao, H. Nakai, T. Vreven, J. R. Montgomery Jr., J. A. Peralta, F. Ogliaro, M. Bearpark, J. J. Heyd, E. Brothers, K. N. Kudin, V. N. Staroverov, R. Kobayashi, J. Normand, K. Raghavachari, A. Rendell, J. C. Burant, S. S. Iyengar, J. Tomasi, M. Cossi, N. Rega, J. M. Millam, M. Klene, J. E. Knox, J. B. Cross, V. Bakken, C. Adamo, J. Jaramillo, R. Gomperts, R. E. Stratmann, O. Yazyev, A. J. Austin, R. Cammi, C. Pomelli, J. W. Ochterski, R. L. Martin, K. Morokuma, V. G. Zakrzewski, G. A. Voth, P. Salvador, J. J. Dannenberg, S. Dapprich, A. D. Daniels, O. Farkas, J. B. Foresman, J. V. Ortiz, J. Cioslowski and D. J. Fox, *Gaussian 09 Revision D.01*, Gaussian Inc. Wallingford CT 2009.
- 53 M. Cossi and V. Barone, *J. Chem. Phys.*, 2001, **115**, 4708–4717.
- 54 F. Avila Ferrer, R. Improta, F. Santoro and V. Barone, *Phys. Chem. Chem. Phys.*, 2011, **13**, 17007–17012.
- 55 A. E. Reed, L. A. Curtiss and F. Weinhold, *Chem. Rev.*, 1988, **88**, 899–926.
- 56 M. Biczysko, J. Bloino, F. Santoro and V. Barone, in *Computational Strategies for Spectroscopy, from Small Molecules to Nano Systems*, ed. V. Barone, Wiley, Chich-

- ester, 2011, pp. 361–443.
- 57 A. Lami and F. Santoro, in *Computational Strategies for Spectroscopy, from Small Molecules to Nano Systems*, ed. V. Barone, Wiley, Chichester, 2011, pp. 475–516.
- 58 J. Franck and E. G. Dymond, *Transactions of the Faraday Society*, 1926, **21**, 536–542.
- 59 E. U. Condon, *Physical Review*, 1926, **28**, 1182–1201.
- 60 E. U. Condon, *Physical Review*, 1928, **32**, 858–872.
- 61 F. J. Avila Ferrer and F. Santoro, *Phys. Chem. Chem. Phys.*, 2012, **14**, 13549–13563.
- 62 P. Macak, Y. Luo and H. Ågren, *Chem. Phys. Lett.*, 2000, **330**, 447–456.
- 63 D. Licari, A. Baiardi, M. Biczysko, F. Egidi, C. Latouche and V. Barone, *J. Comput. Chem.*, 2015, **36**, 321–334.
- 64 H. Kobayashi, M. Ogawa, R. Alford, P. L. Choyke and Y. Urano, *Chem. Rev.*, 2010, **110**, 2620–2640.
- 65 P. Siejak and D. Frackowiak, *J. Phys. Chem. B*, 2005, **109**, 14382–14386.
- 66 W. G. van Sark, *Renewable Energy*, 2013, **49**, 207 – 210.
- 67 M. G. Debijs and P. P. C. Verbunt, *Advanced Energy Materials*, 2012, **2**, 12–35.
- 68 J. Digaum and S. M. Kuebler, *Proc. SPIE*, 2014, **8981**, 89810E–89810E–11.

	λ_{abs} [nm]	ϵ [$M^{-1}cm^{-1}$]	λ_{em} [nm]	S [nm]	Φ_f^a	B [$M^{-1}cm^{-1}$] ^b
1a	367	17'000	517	150	0.10	1'700
2a	329	36'000	408	79	0.61	21'960
1b	373	15'000	538	165	0.10	1'500
2b	331	27'000	422	91	0.51	13'770

^a Fluorescence quantum yield (Φ) was determined relative to quinine sulphate in 0.1M H₂SO₄ ($\Phi = 0.54$).

^b The brightness (B) of fluorophores are calculated as the product of the absorption coefficient ϵ and Φ .

	S_0	S_1
1a	-36	-6
2a	-39	-8
1b	-36	-10
1b'	-36	-10
2b	-39	-10
2b'	-38	-8

Table 1 Spectroscopic properties of functionalised **1** fluorophores dissolved in THF

	B3LYP	B3LYP/PCM(THF)	CAM-B3LYP/PCM(THF)
1a	449	494	349
2a	374	385	315
1b	476	530	357
1b'			356
2b	387	401	319
2b'			321

Table 2 Vertical absorption energies (in nm) of the first bright electronic transition computed with B3LYP, B3LYP/PCM(THF) and CAM-B3LYP/PCM(THF) for **1** and **2** derivatives. In all cases computations are performed in conjunction with the SNSD basis set.

	λ_{abs} [nm]	f	λ_{em} [nm]	f	S [nm]
THF solution					
1a	349	1.11	449	1.52	100
2a	314	1.57	402	1.80	88
1b	357	1.11	465	1.56	108
1b'	356	1.08	462	1.52	106
2b	319	1.67	410	1.88	91
2b'	321	1.53	412	1.77	91
PMMA					
1a	346	1.19	426	1.37	80
1b'	353	1.16	438	1.35	85

Table 3 Vertical absorption and emission wavelengths and relative oscillator strengths for **1** and **2** derivatives calculated at TD-CAM-B3LYP/SNSD level, in THF solution and PMMA matrix.

Table 4 Dihedral angles (in degrees) between the imidazole and the phenyl-pull moiety (see Fig.4) in the ground state (S_0) and in the excited state (S_1) for **1** and **2** derivatives.

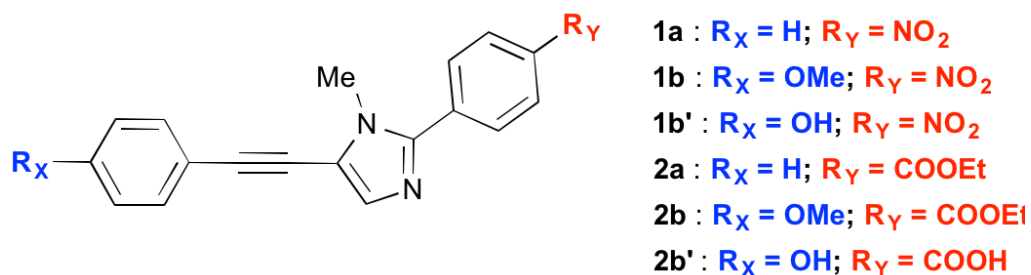
	Transition	λ_{emi} [nm]	f
1b' /THF	HOMO→LUMO (88%)	462	1.5201
	HOMO-7→LUMO (81%)	350	0.0005
	HOMO→LUMO+1 (77%)	303	0.3706
1b' /PMMA	HOMO→LUMO (86%)	438	1.3535
	HOMO-7→LUMO (83%)	349	0.0049
	HOMO→LUMO+1 (82%)	308	0.4608
2b' /THF	HOMO→LUMO (92%)	441	1.7726
	HOMO→LUMO+1 (81%)	296	0.1763
	HOMO-3→LUMO (51%)	272	0.0020
	HOMO→LUMO+4 (31%)		

Table 5 Vertical emission wavelengths and relative oscillator strengths for the lowest transitions of **1b'** and **2b'** derivatives calculated at TD-CAM-B3LYP/SNSD level, in THF solution and PMMA matrix.

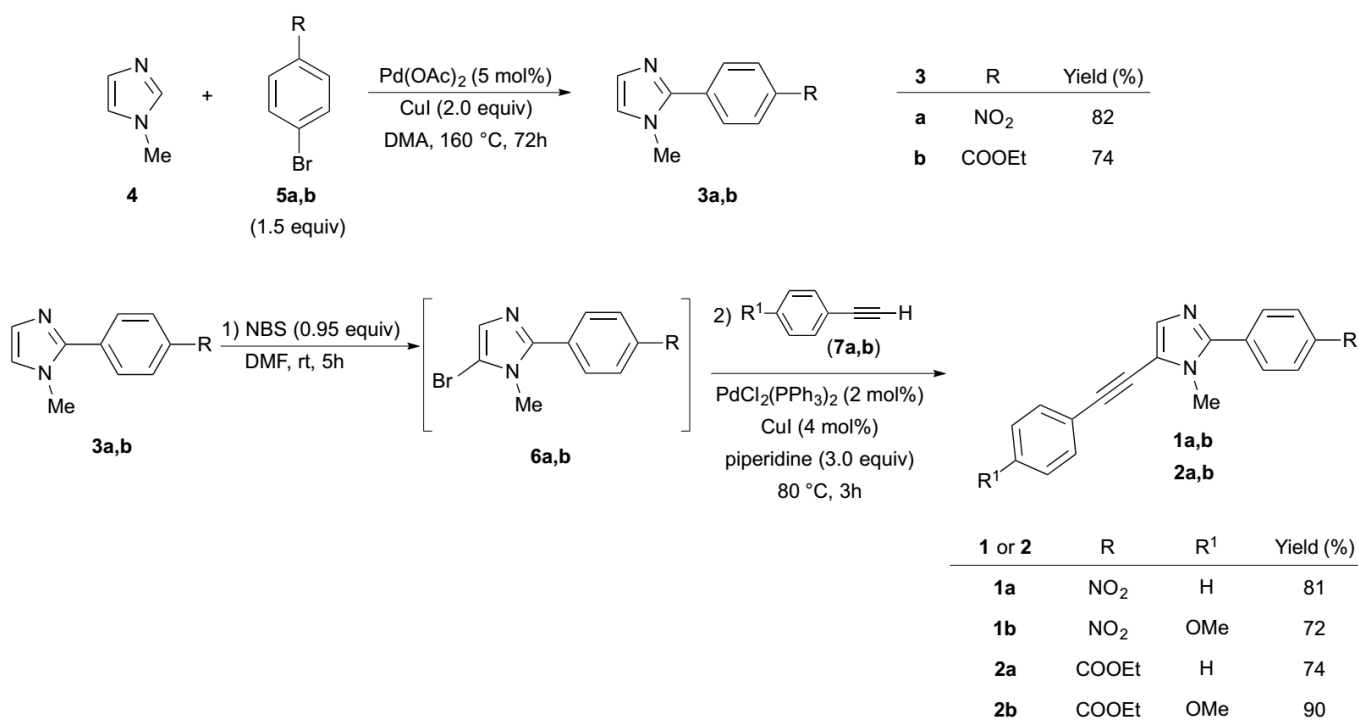
	λ_{abs} [nm]	λ_{em} [nm]	S [nm]	Φ_f^a
1a /PMMA	367	517	150	0.1
1b /PMMA	373	519	146	0.1

^a Fluorescence quantum yield (Φ) was determined relative to 9,10-diphenylanthracene in PMMA ($\Phi_f^a = 0.83$).

Table 6 Spectroscopic properties of **1a**/PMMA and **1b**/PMMA thin films



Scheme 1 Scheme of the **1** and **2**-derivatives skeletal formula, characterized by a phenylethynyl-phenylimidazole backbone and different push (R_X) and pull (R_Y) groups.



Scheme 2 Synthesis of fluorophores **1a,b** and **2a,b**.

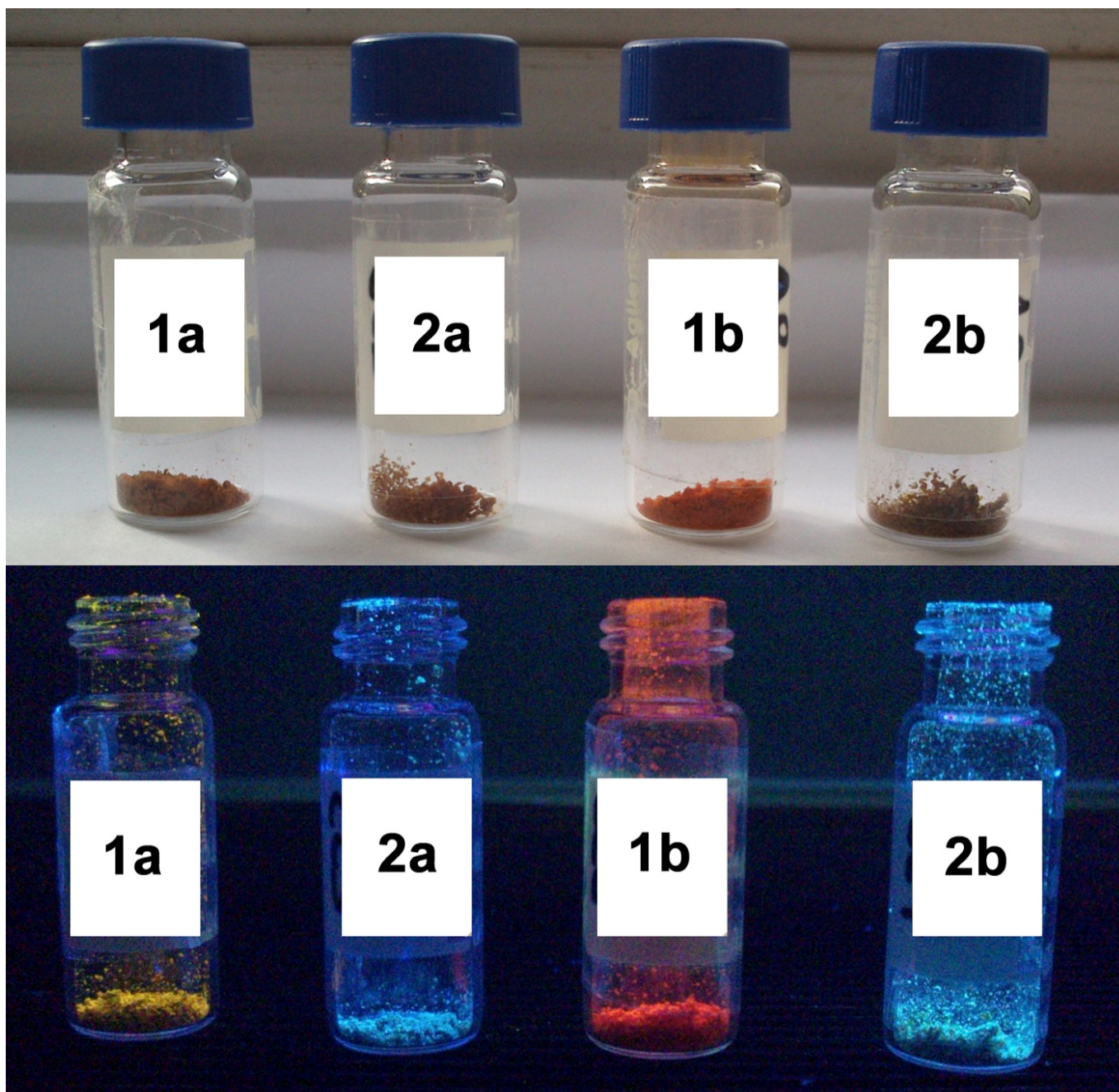


Fig. 1 Fluorophores **1a,b** and **2a,b** in the form of solid powders under visible (up) and near-UV light (366 nm, down).

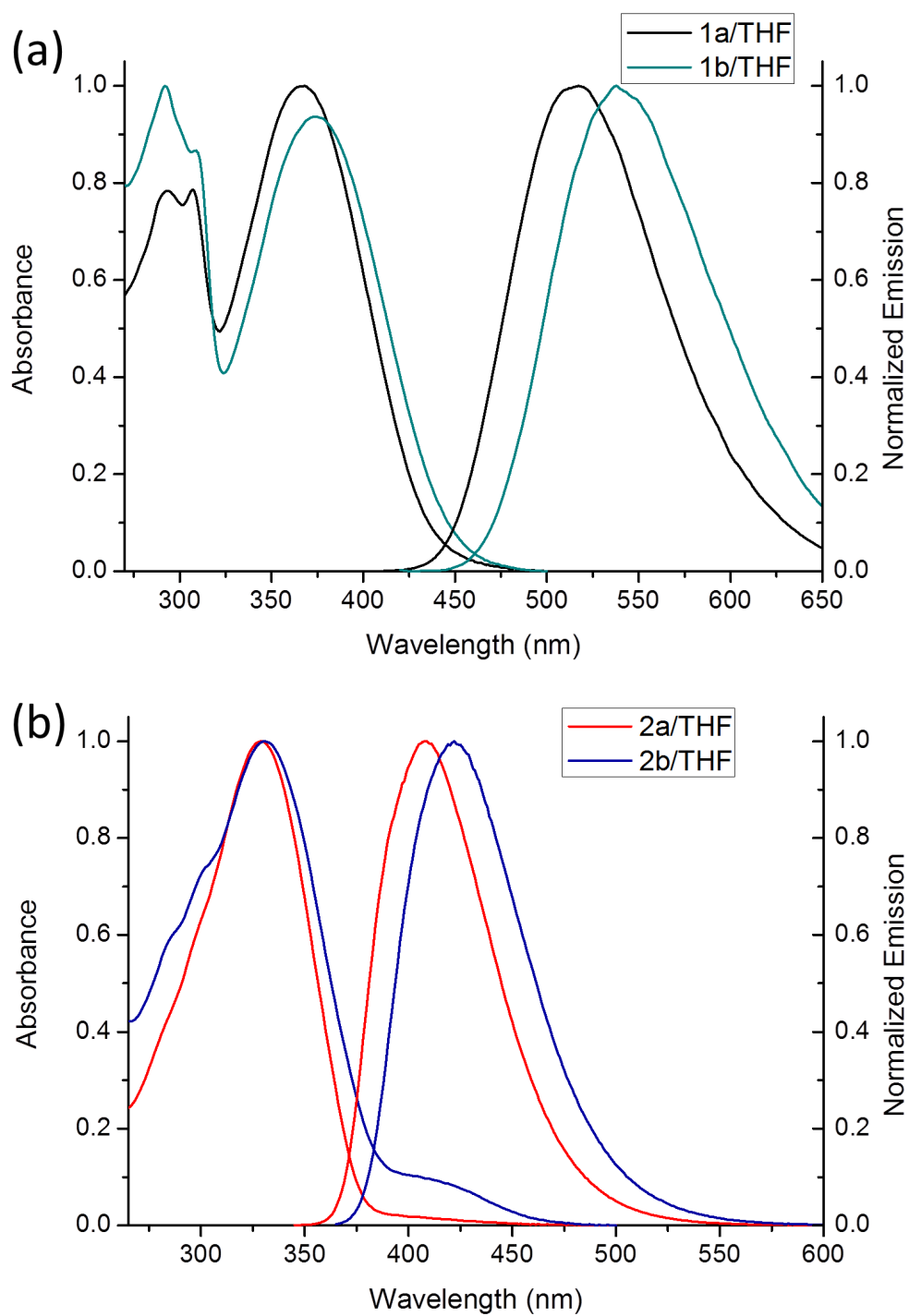


Fig. 2 Absorbance (left) and emission (right) spectra of $5\mu\text{M}$ (a) **1a** and **1b** and (b) **2a** and **2b** solutions in THF.

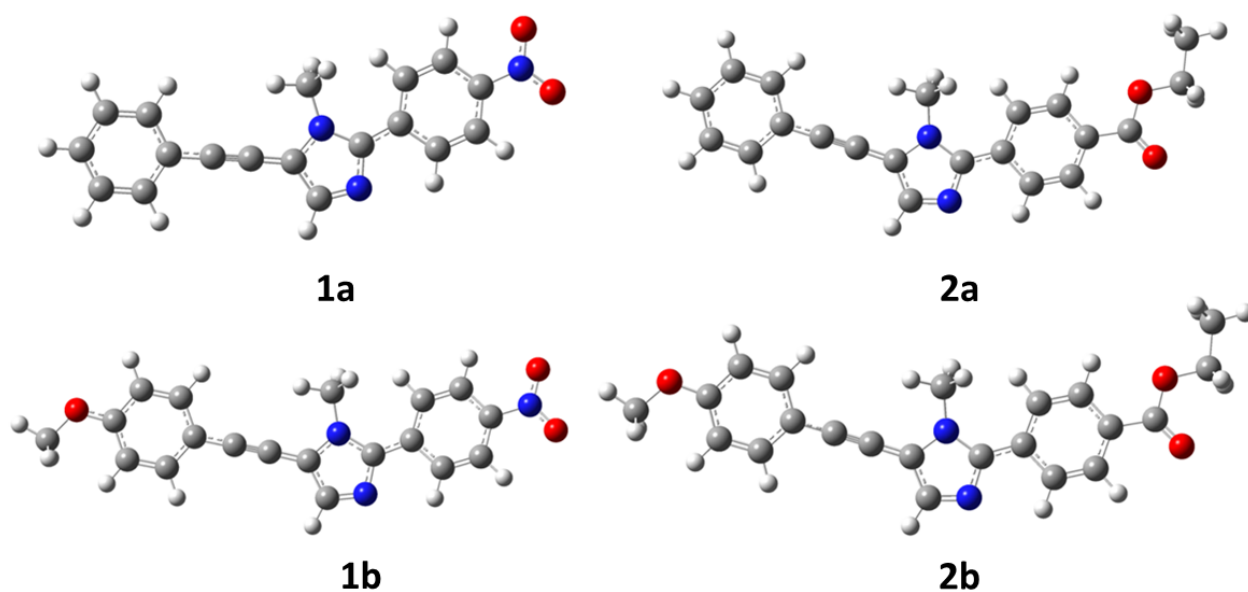


Fig. 3 Ground state optimized structures for 1- and 2-derivatives computed at CAM-B3LYP/PCM(THF) level of theory.

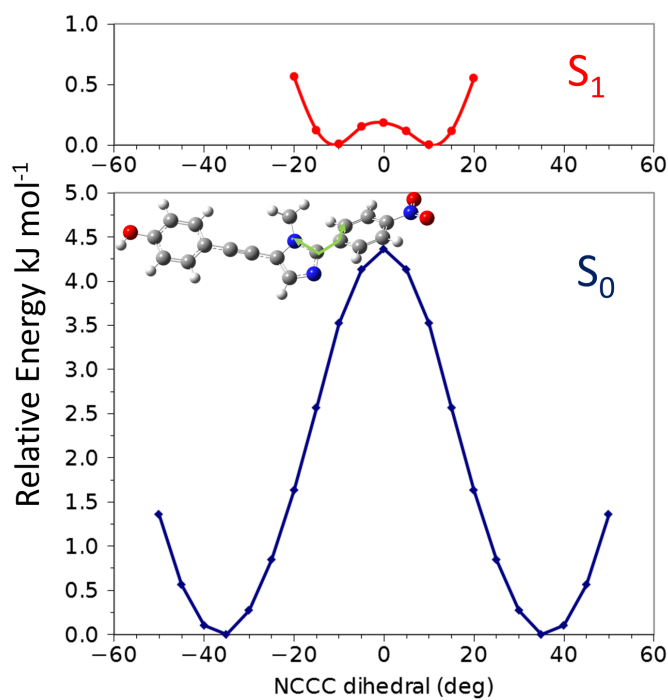


Fig. 4 Relaxed Potential Energy Profile scan along the dihedral angle (marked in green) between the imidazole and the phenyl-pull moiety for the ground state (S_0) and the excited state (S_1) of the **1b'** chromophore.

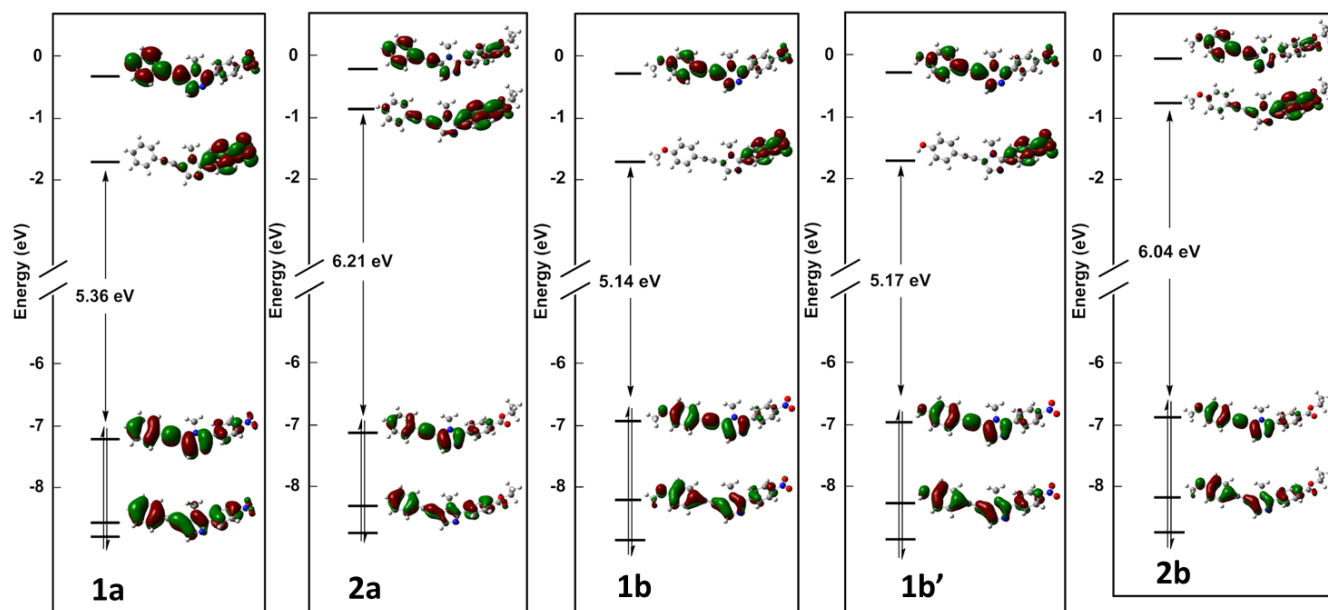


Fig. 5 MOs diagrams of 1- and 2-derivatives obtained at CAM-B3LYP/PCM(THF) level of theory.

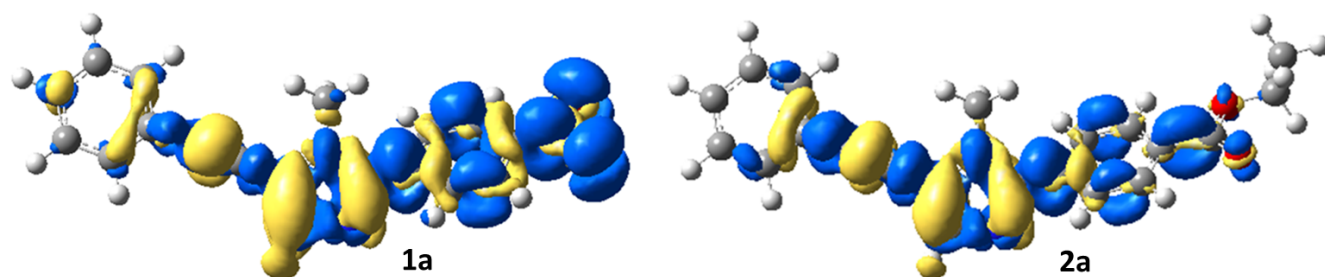


Fig. 6 Plots of the difference in electron density (ELD) between the ground state and the first excited electronic state both in the equilibrium geometry of the ground state for the **1a** and **2a** chromophores computed at CAM-B3LYP/PCM(THF) level of theory. The regions that have lost electron density as a result of transition are shown in yellow, whereas the blue regions have gained electron density. ELD densities were plotted with an isovalue threshold of 0.001.

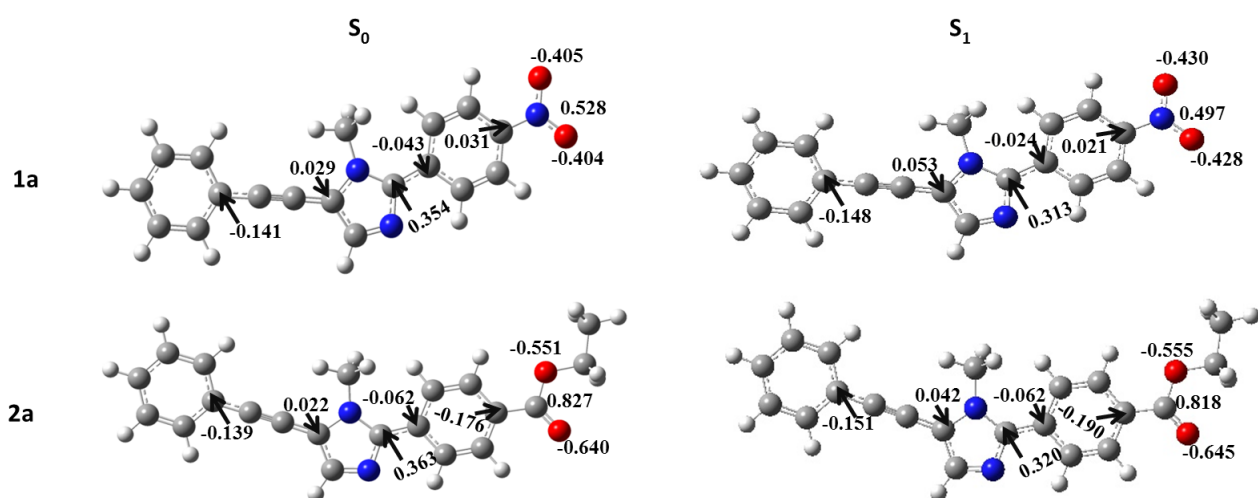


Fig. 7 Selected atomic charges from natural bond orbital analysis for the **1a** and **2a** chromophores. Values computed at CAM-B3LYP/SNSD/PCM(THF) and TD-CAM-B3LYP/SNSD/PCM(THF) levels of theory for the ground and excited states, respectively.

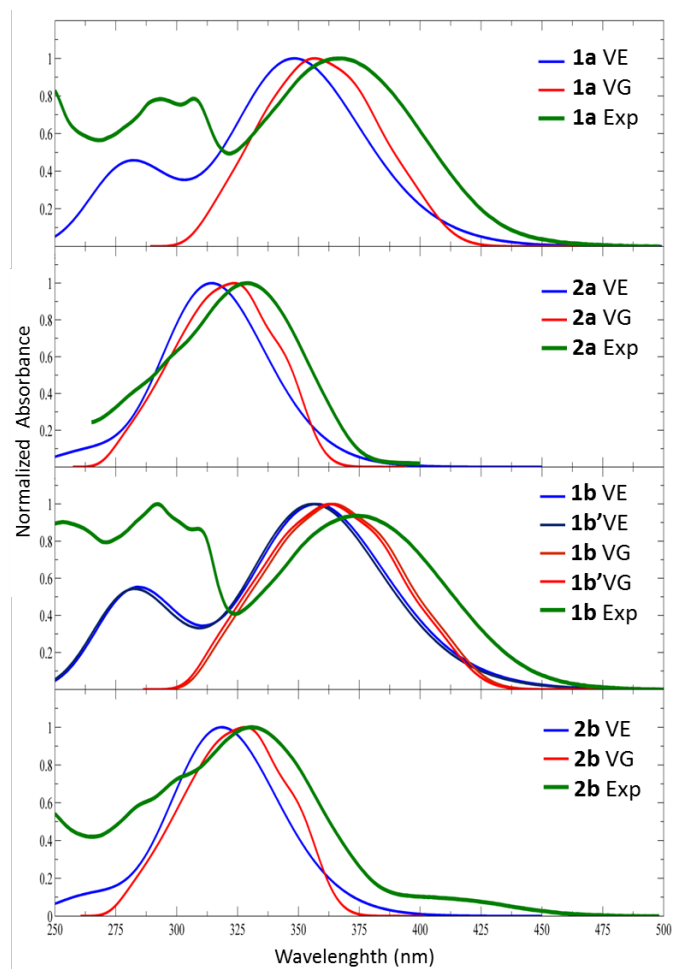


Fig. 8 Normalized simulated electronic (VE approach) and vibronic (VG approach) absorption spectra for the 1- and 2-derivatives, compared with the experimental absorption spectra. The theoretical spectra line-shapes have been convoluted using Gaussian functions with a half-width at half-maximum (HWHM) of 2500 cm^{-1} for the electronic spectra and 750 cm^{-1} for the vibronic ones.

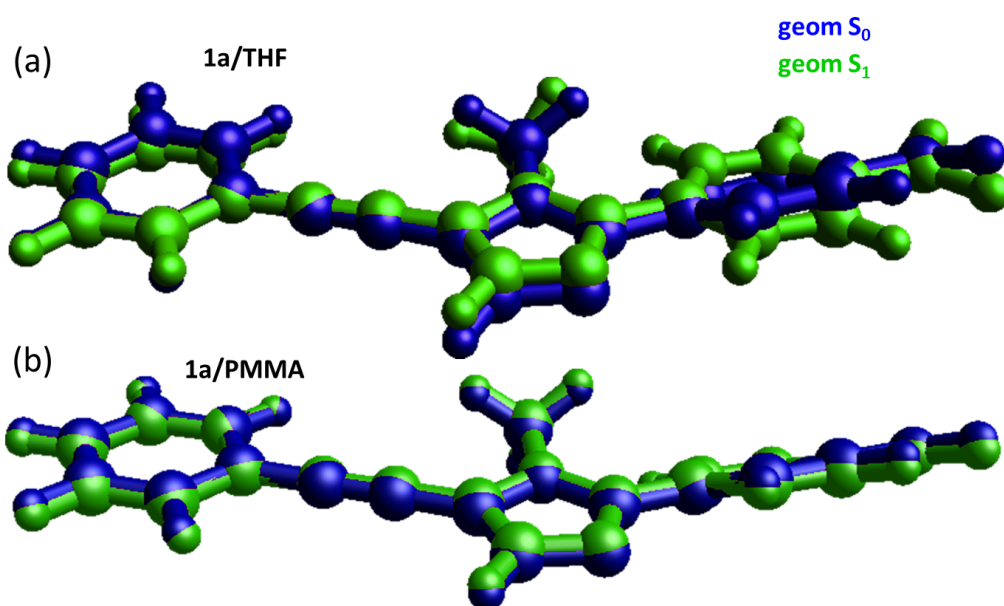


Fig. 9 Superposition of the ground (blue) and excited state (green) equilibrium structures of the **1a** (a) in the THF solution and (b) in the PMMA.

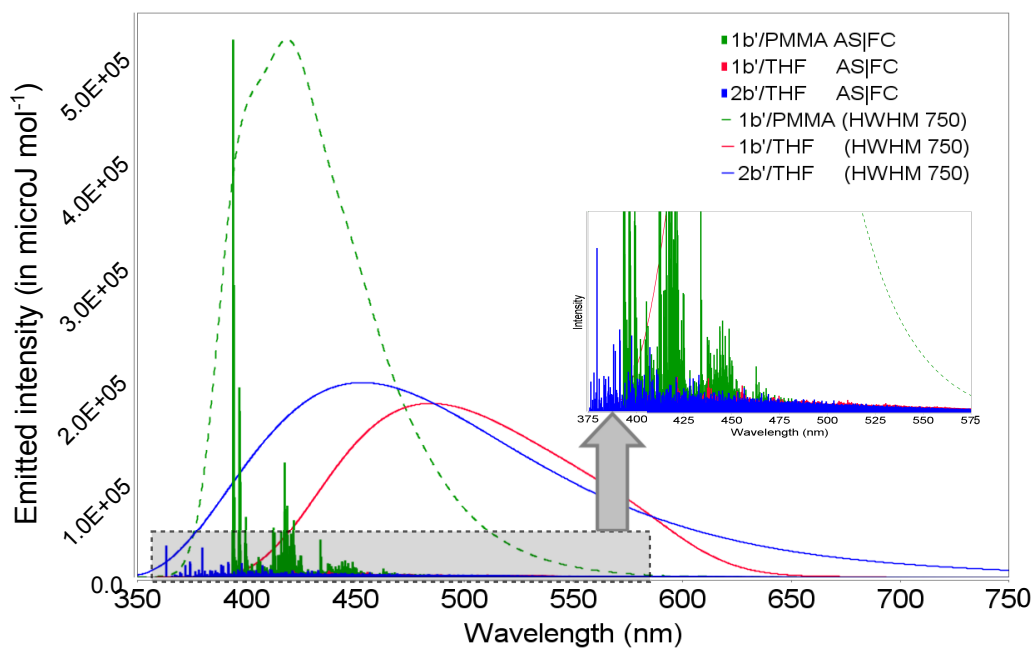


Fig. 10 Simulated vibronic (AS approach) emission spectra for **1b'** and **2b'** chromophores in THF and in PMMA. The theoretical stick-spectra have been convoluted using Gaussian functions with a half-width at half-maximum (HWHM) of 750 cm⁻¹.

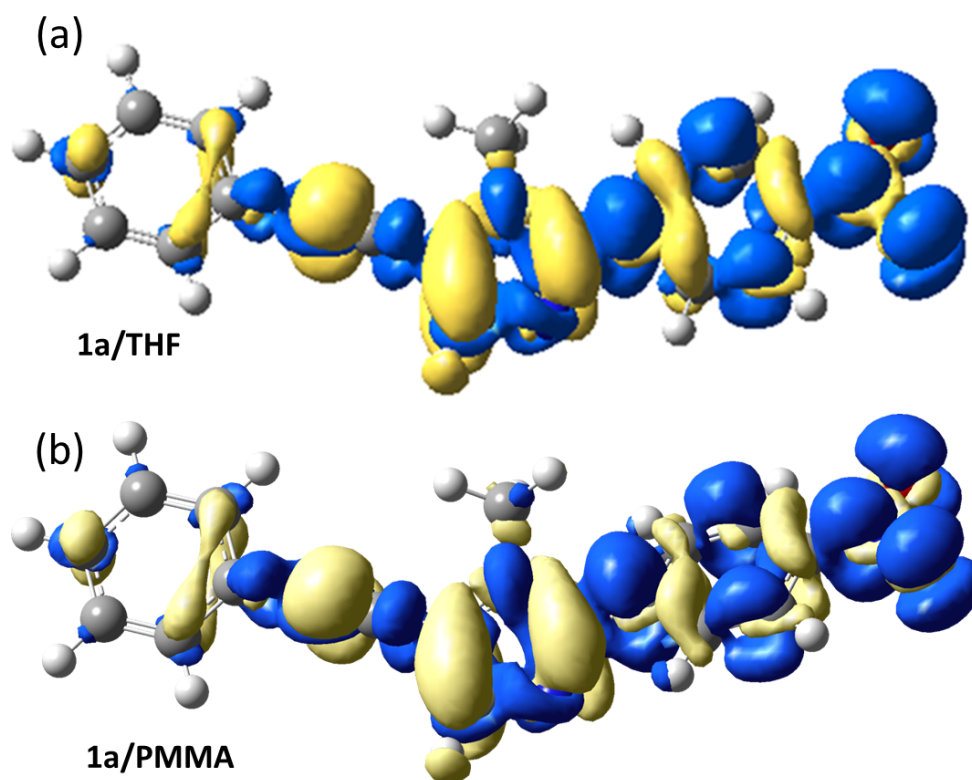


Fig. 11 Plots of the difference in electron density (ELD) between the ground state and the first excited electronic state of the **1a**, at the excited state equilibrium geometry (a) in THF and (b) in PMMA computed at CAM-B3LYP/PCM(THF) level of theory. The regions that have lost electron density as a result of transition are shown in yellow, whereas the blue regions have gained electron density. ELD densities were plotted with an isovalue threshold of 0.001.

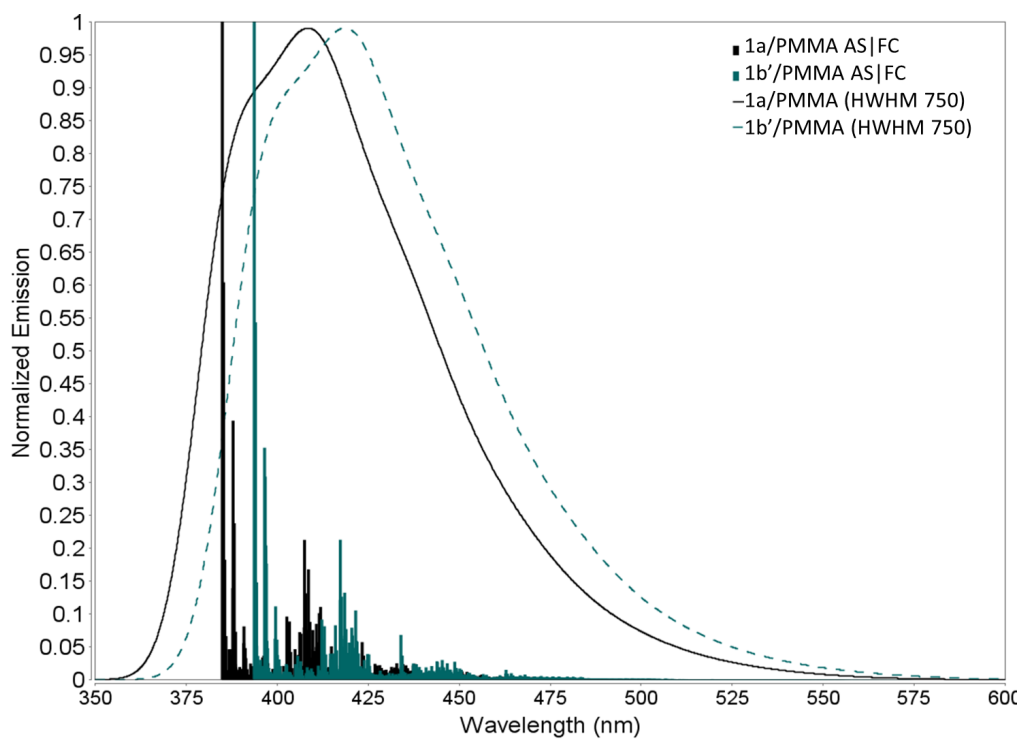


Fig. 12 Normalized simulated vibronic (AS approach) emission spectra for **1a** and **1b'** chromophores in PMMA. The theoretical stick-spectra have been convoluted using Gaussian functions with a half-width at half-maximum (HWHM) of 750 cm⁻¹.

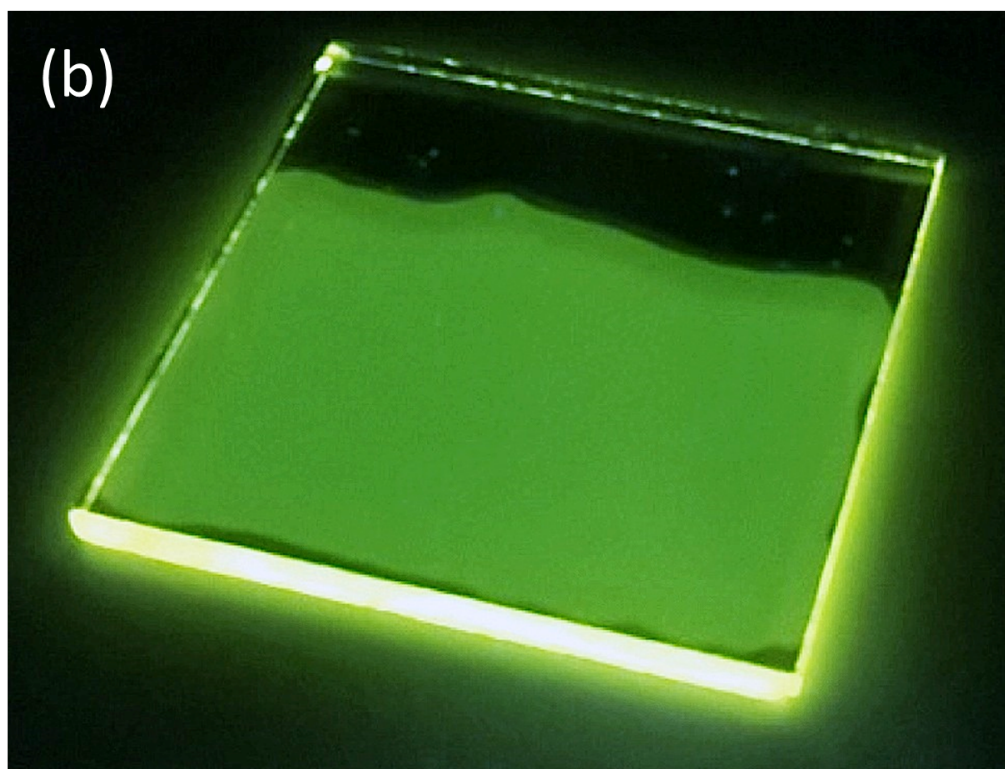
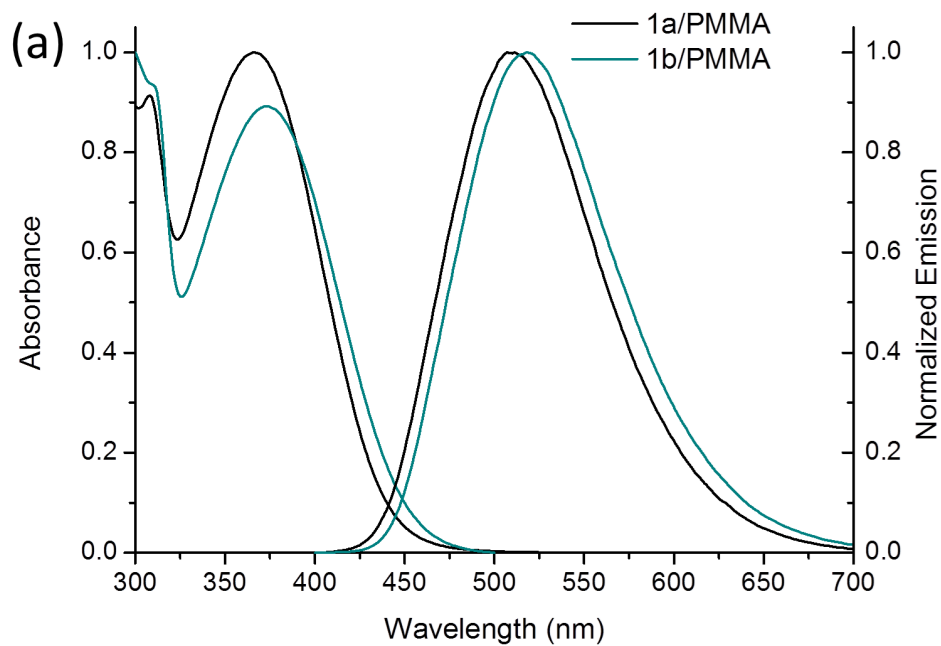


Fig. 13 Upper panel: Absorbance (left) and emission (right) spectra of 1 wt.% **1a**/PMMA and **1b**/PMMA thin films ($25\pm 5 \mu\text{m}$); Lower panel: An optically pure 50x50x3 mm glass coated with a $25\pm 5 \mu\text{m}$ thick **1b**/PMMA film.

TOC: Integrated experimental and computational investigation on absorption and emission spectra of the novel organic fluorophores in the solution and in polymer environment give insights for their potential application in luminescent solar concentrators.

